

Redshift Classification of Optical Gamma-Ray Bursts using Supervised Learning

Milind Sarkar ^a, Maria Giovanna Dainotti ^{b,c,d,e}, Nikita S. Khatiya ^f, Dhruv S. Bal ^f, Malgorzata Bogdan ^g, Ye Li ^h, Agnieszka Pollo ^{i,j}, Dieter H. Hartmann ^f, Bing Zhang ^e, Simanta Deka^k, Nissim Fraija ^l, J. Xavier Prochaska ^{b,m,n}

^aDepartment of Physical Sciences Indian Institute of Science Education and Research (IISER) Mohali Punjab India

^bDivision of Science National Astronomical Observatory of Japan 2-21-1 Osawa Mitaka Tokyo 181-8588 Japan

^cDepartment of Astronomical Sciences The Graduate University for Advanced Studies SOKENDAI Japan

^dSpace Science Institute 4765 Walnut Street Suite B Boulder CO 80301 USA

^eNevada Center for Astrophysics University of Nevada 4505 Maryland Parkway Las Vegas NV 89154 USA

^fDepartment of Physics & Astronomy Clemson University Clemson SC 29634 USA

^gUniversity of Wroclaw Wroclaw Poland

^hPurple Mountain Observatory Chinese Academy of Sciences Nanjing 210023 China

ⁱNational Centre for Nuclear Research 02-093 Warsaw Poland

^jJagiellonian University Krakow Poland

^kDepartment of Physics Gauhati University Guwahati 781014 Assam India

^lInstituto de Astronomia Universidad Nacional Autonoma de Mexico Circuito Exterior C.U. A.P. 70-264 Mexico

^mUniversity of California Santa Cruz 1156 High Street Santa Cruz, CA 95064 USA

ⁿKavli Institute for the Physics and Mathematics of the Universe (Kavli IPMU) 5-1-5 Kashiwanoha Kashiwa 277-8583 Japan

17 Dec 2025

arXiv:2512.13038v2 [astro-ph.HE]

Abstract

Gamma-ray bursts (GRBs) are among the most luminous explosions in the Universe and serve as powerful probes of the early cosmos. However, the rapid fading of their afterglows and the scarcity of spectroscopic measurements make photometric classification crucial for timely high-redshift (high- z) identification. We present an ensemble machine learning framework for redshift classification of GRBs based solely on their optical plateau and prompt emission properties. Our dataset comprises 171 long GRBs observed by the *Swift* UVOT and over 450 ground-based telescopes. The analysis pipeline integrates reliable statistical techniques, including M-estimator outlier rejection, multivariate imputation via Multiple Imputation by Chained Equations (MICE), and Least Absolute Shrinkage and Selection Operator (LASSO) feature selection, followed by a SuperLearner ensemble combining parametric, semi-parametric, and non-parametric algorithms. The optimal model — trained on raw optical data with outlier removal at the redshift threshold, z_t at $z = 2.0$ - achieves a true positive rate of 74% and an Area Under the Curve (AUC) of 0.84, maintaining balanced generalization between training and test sets. At higher thresholds ($z_t = 3.0$), the classifier sustains strong discriminative power with an AUC of 0.88. Validation on an independent GRB sample yielded 97% overall accuracy, perfect specificity, and an ensemble AUC of 0.93. Compared to previous prompt- and X-ray-based classifiers, our optical framework offers enhanced sensitivity to high- z events, improved reliability against data incompleteness, and greater applicability to ground-based follow-up. With this study, we publicly release a web application that allows real-time redshift classification, enabling rapid identification of candidate high- z GRBs and facilitating their use as cosmological probes.

Keywords: Gamma Ray Bursts, Machine Learning, Statistical Learning

1. Introduction

Gamma-ray bursts (GRBs) are among the most energetic phenomena in the universe. GRBs emit radiation across the entire electromagnetic spectrum and are categorized into two classes: Long-duration (LGRBs) and Short-duration GRBs (SGRBs) based on their T_{90} value, which represents the time interval containing 90% of the total background-subtracted gamma-ray prompt fluence, measured from 5% to 95% of the cumulative fluence (Kouveliotou et al., 1993; Mazets et al., 1981). LGRBs have $T_{90} > 2$ seconds, while SGRBs have $T_{90} < 2$ seconds.

However, an intermediate class of GRBs, the short with extended emission, with long duration, but with spectral properties similar to the short GRBs, have been discovered in 2006,

(Norris and Bonnell, 2006). To address this limitation, a new classification scheme was proposed by (Zhang and Mészáros, 2004; Zhang et al., 2006, 2009; Zhang et al., 2014), distinguishing GRBs into Type I and Type II categories, where Type I GRBs are typically associated with compact object mergers, such as neutron star mergers, whereas Type II GRBs are associated with core-collapse supernova.

However, the recent discovery of LGRBs associated with Kilonovae (KNe) (Rastinejad et al., 2022) and SGRBs linked to core collapse SNe (Ahumada et al., 2021) has made the classification of Type I and II GRBs, even more challenging.

From an observational perspective, a GRB consists of two distinct phases. The first is the prompt emission, which is typically detected in γ -rays, hard X-rays, soft X-rays, and occasionally in the optical band (Vestrand et al., 2005; Oganessian et al., 2019; Shen and Zhang, 2009). The second phase is the

*Corresponding author: maria.dainotti@nao.ac.jp

afterglow, observed as the counterpart emission in hard and soft X-rays, optical wavelengths, and sometimes in the radio band (Vestrand et al., 2005; Beskin et al., 2010; Gorbovskoy et al., 2012; Vestrand et al., 2014; Zhang, 2014, 2018; Costa et al., 1997; van Paradijs et al., 1997; Piro et al., 1998; Kumar and Zhang, 2015).

A prominent feature often observed in the light curves (LCs) of GRBs is the plateau phase, which is characterized by a relatively constant flux preceding the subsequent decay of the afterglow (O’Brien et al., 2006; Zhang et al., 2006; Nousek et al., 2006; Sakamoto et al., 2007; Liang et al., 2007; Dainotti et al., 2008; Zaninoni et al., 2013; Rowlinson et al., 2014). Plateau phases are detected in approximately in 38.5% of X-ray afterglows (Evans et al., 2009; Li et al., 2018; Srinivasaragavan et al., 2020; Dainotti et al., 2021; Narendra et al., 2025), 30% of optical afterglows (Vestrand et al., 2005; Kann et al., 2006; Zeh et al., 2006; Panaitescu and Vestrand, 2008, 2011; Oates et al., 2012; Dainotti et al., 2020a, 2022a), and 6.6% of radio afterglows (Levine et al., 2022).

GRBs have been observed at redshifts (z) as high as $z \sim 9.4$ (Cucchiara et al., 2011), and theoretically, they could be detected up to $z \sim 20$ (Lamb and Reichart, 2000; Lamb, 2002). This makes GRBs invaluable tools for probing the evolution of the early Universe. They can provide insights into key phenomena such as the epoch of reionization (Fausey et al., 2024), the formation of Population III stars (Toma et al., 2016; Bromm and Loeb, 2006), and star formation rates at very high- z (Li, 2008; Wang, 2013). Additionally, GRBs can also shed light on the metal and dust content of early, faint galaxies (Frail et al., 2006; Cusumano et al., 2007, 2006). However, to fulfill this potential of GRBs, we require spectroscopic redshift measurements of high- z GRBs.

The Neil Gehrels *Swift* Observatory (*Swift* (Gehrels et al., 2004)) has revolutionized our understanding of high- z GRBs with its precise localization capabilities over its two decades of operation. The *Swift* satellite is equipped with three primary instruments: the Burst Alert Telescope (BAT, 15–150 keV, (Burrows et al., 2005)), which detects the prompt emission; the X-ray Telescope (XRT, 0.2–10 keV, (Barthelmy et al., 2005)), enabling rapid follow-up observations of the afterglow; and the Ultraviolet/Optical Telescope (UVOT, 1700–6500Å, (Roming et al., 2005)), which observes in ultraviolet and optical wavelengths. However, the rapid dimming of GRB afterglows presents a significant challenge, as follow-up observations of even optically bright GRBs are subject to limited telescope time. Hence, even with *Swift*’s remarkable observational capabilities, only 26% of its GRB catalog has redshift measurements as of this writing. The 26% is an estimate that takes into consideration all GRBs, both from Fermi and *Swift*. The estimate has been calculated taking into account the Greiner webpage. Thus, there is a clear necessity to develop alternative methods for increasing the sample size of GRBs with reliable redshift measurements.

This low fraction is driven primarily by observational and astrophysical selection effects rather than instrumental limitations. GRB afterglows fade rapidly, often before spectroscopic follow-up can be obtained, and a substantial fraction of events are optically faint or “dark” due to dust extinction in their host

galaxies or absorption at high redshift. Several studies have shown that a substantial fraction of GRBs —of order half— are optically faint or dark, rendering them inaccessible to afterglow-based spectroscopic redshift measurements even with prompt follow-up (e.g. Prochaska et al. (2006, 2007, 2008, 2009); Perley et al. (2009, 2013); Greiner et al. (2011)). These effects impose a limitation on redshift completeness even for well-localised bursts. In many cases, reliable redshift recovery therefore relies on the identification of the GRB host galaxy using accurate X-ray or optical localisations, followed by deep, late-time spectroscopy of the host (Perley et al., 2009, 2013). The present work is not intended to replace spectroscopic or host-galaxy redshift measurements, but to provide probabilistic redshift information and population-level constraints for GRBs that would otherwise remain unclassified.

One approach that can alleviate this bottleneck is to develop a system capable of quickly identifying whether a newly detected GRB is a high- z event or not. Then, quick follow-up observations can be initiated to capture the events flagged as high- z . Although past studies have attempted to identify/predict high- z GRBs using empirical relations between GRB properties, the results have not been sufficiently accurate (Grupe et al., 2007; Campana et al., 2007; Salvaterra et al., 2007; vanden Berk et al., 2008; Ukwatta et al., 2008, 2009; Koen, 2009, 2010; Dainotti et al., 2011). (Morgan et al., 2012; Ukwatta et al., 2016) have previously employed supervised machine learning (ML) techniques to identify high- z GRBs. (Morgan et al., 2012) attempted to classify 135 *Swift* LGRB into high- z ($z > 4$) and low- z events, using the Random Forest algorithm (Hastie et al., 2009; Breiman, 2001). Based on this, they claim that their top 40% of predicted candidates capture $\approx 84\%$ of high- z bursts. (Ukwatta et al., 2016) performed a Random Forest regression analysis using *Swift* LGRBs and achieved a Pearson correlation (r) of 0.57.

More recently, (Dainotti et al., 2024a) used an ML-based analysis to determine the redshift of *Swift* LGRBs, used a subset of those exhibiting X-ray plateau, and achieved an $r = 0.93$. Using the trained ML model, they predicted the redshift of 150 LGRBs. (Dainotti et al., 2024b) used a subset of LGRBs exhibiting optical plateau and also achieved an $r = 0.93$. They also demonstrated the feasibility of using ML-based redshift estimates in determining the luminosity function and density rate evolution of LGRBs.

In this work, we use the same set of LGRBs exhibiting optical plateau, and we classify them based on their redshift, using an ensemble among several ML models. The objective is to develop a reliable method to guide follow-up programs in the optical domain. Here, we aim to classify the high- z nature of GRBs within hours of their discovery, using properties specifically associated with the prompt and plateau emission phases. We use a sample of 171 LGRBs (27% larger than used by (Morgan et al., 2012)). This paper serves as a counterpart to (Dainotti et al., 2024a), shifting the focus to optical properties of GRBs and exploring their potential to provide complementary insights into fundamental GRB physics and redshift determination over X-rays. Using optical GRBs for redshift classifier is the novelty of this work. While X-ray observations are crucial for ini-

tial GRB detection and characterization, the majority of redshift determinations during *Swift* follow-ups are performed using optical telescopes, highlighting their central role in GRB studies (Roming et al., 2006; Levesque et al., 2010; Berger, 2008). Thus, optical observations, particularly of plateaus, can provide a more accurate method for detecting high- z GRBs.

The paper is structured as follows. In Section 2, we describe the data sample and the features used in our analysis. Section 3 provides a detailed explanation of our methodology, including outlier removal, data imputation, feature selection, the machine learning algorithms utilized, and the implementation of the SuperLearner. The results of the SuperLearner classification are presented in Section 4. In Section 5, we discuss our findings, followed by a comparison with prior work in Section 5.3. Finally, we summarize and conclude in Section 7.

2. Data Sample

In this study, we used the sample of 171 LGRBs from (Dainotti et al., 2024b). These LGRBs were observed by *Swift* UVOT and from 455 ground-based telescopes/detectors, e.g., the Subaru Telescope, Gamma-ray Burst Optical/Near-IR Detector, Reionization and Transients Infrared Camera/Telescope, and the MIT-SuME Telescope. The data contains measurements of the following observed properties in the optical wavelengths:

1. z - the GRB's redshift.
2. T_{90} - the duration over which 90% of the total γ -ray observed fluence of the GRB is emitted.
3. F_a - the flux at the end of the plateau emission.
4. T_a - the time at the end of the plateau emission.
5. α - the power-law decay index observed after the end of the plateau emission.
6. β - the spectral index derived from the plateau emission phase, assuming a power-law distribution of the spectral energy.
7. NH - the column density of neutral hydrogen along the line of sight.
8. Fluence - the energy fluence of the prompt emission during T_{90} , measured in erg cm^{-2} .
9. PeakFlux - the peak photon flux during the prompt emission, expressed in photons cm^{-2} .
10. PhotonIndex - the prompt photon index derived from modeling the BAT Telescope's photon energy distribution using a power-law.

Out of the above-mentioned properties, four properties, namely, T_{90} , Fluence, PeakFlux, and PhotonIndex are part of the prompt emission. Five properties, namely, T_a , F_a , α , β , and NH, belong to the optical plateau and afterglow phase. The optical plateau parameters used here are obtained from (Dainotti et al., 2022b).

To address the broad distribution of the properties, we use the base-10 logarithm values of T_{90} , Fluence, PeakFlux, NH, F_a , and T_a . Additionally, we set up a filtering criteria for our data following the procedure of (Dainotti et al., 2024a), where we assign N/A to the values where $\log(\text{NH}) < 21$, $\text{PhotonIndex} < 0$, $\text{PeakFlux} = 0$, $\alpha > 3$, and $\beta > 3$. These thresholds are used

because such values are non-physical or unusual for the majority of the LGRB sample (for example, the $\alpha > 3$ and $\beta > 3$ belong to the tail of their respective distributions). We later impute these N/A values in our analysis using a data imputation technique, as described in Section 3.2. This is done so that we can retain the maximum size for our training set. For our response variable, which the ML model will predict, we use $\log(z + 1)$ as it offers a more natural parametrization of the cosmological variable z and results in improved ML performance.

In our analysis, we used 80% of the available GRBs as our training set and the rest 20% as our test set, selected randomly.

In contrast to (Dainotti et al., 2024a), which uses LGRBs exhibiting X-ray plateau, we use LGRBs exhibiting optical plateau for our analysis. The optical plateau is typically observed within the first few hours to a day after the burst and is characterized by features similar to those of the X-ray plateaus (Dainotti et al., 2020b).

3. Methodology

In this section, we describe four techniques implemented in our analysis; see Figure 1. As is evident from Fig. 1, we present four results for our ML model's performance, which differ based on which technique (outlier removal, data imputation, feature selection, and algorithm selection for the SuperLearner ensemble) is applied to the data. Thus, in the following subsections, we describe the individual techniques, and then we describe the four scenarios for which the results are presented.

3.1. Outlier Removal

Our dataset contains outliers that could affect our ML model's predictions, as they may not be representative of the full GRB sample. Thus, to improve reliability, we apply the M-estimator technique for removing outliers. M-estimator is a generalized maximum likelihood method (Huber, 1964a, 1996; de Menezes et al., 2021) and a reliable alternative to the ordinary least squares (OLS) method. Unlike OLS, which overestimates the influence of outliers, the M-estimator minimizes a function of residuals using the Huber function (Huber, 1964b; Huber and Ronchetti, 2009). This approach uses a generalized linear model (GLM, Nelder and Wedderburn, 1972b), incorporating squared terms of features to capture nonlinear correlations with z . The formula used for the M-estimator outlier removal is as follows:

$$\begin{aligned} \log(1 + z) = & \left((\log \text{PeakFlux})^2 + (\log \text{NH})^2 + (\text{PhotonIndex})^2 \right. \\ & \left. + \beta^2 + \log \text{PeakFlux} + \alpha \right)^2 \\ & + \log F_a + \log T_a + \beta + \text{PhotonIndex} + \log \text{NH} \\ & + (\log F_a)^2 + (\log T_a)^2 + \beta^2. \end{aligned} \quad (1)$$

This formula comes from Equation 1 in Dainotti et al. (2024b). Because the smoothing functions are 1, this is equivalent to use GLM instead of Generalized Additive Model (GAM, (Hastie and Tibshirani, 1987)). This equation is an empirical formula derived from the methodology used in that paper where 161,000

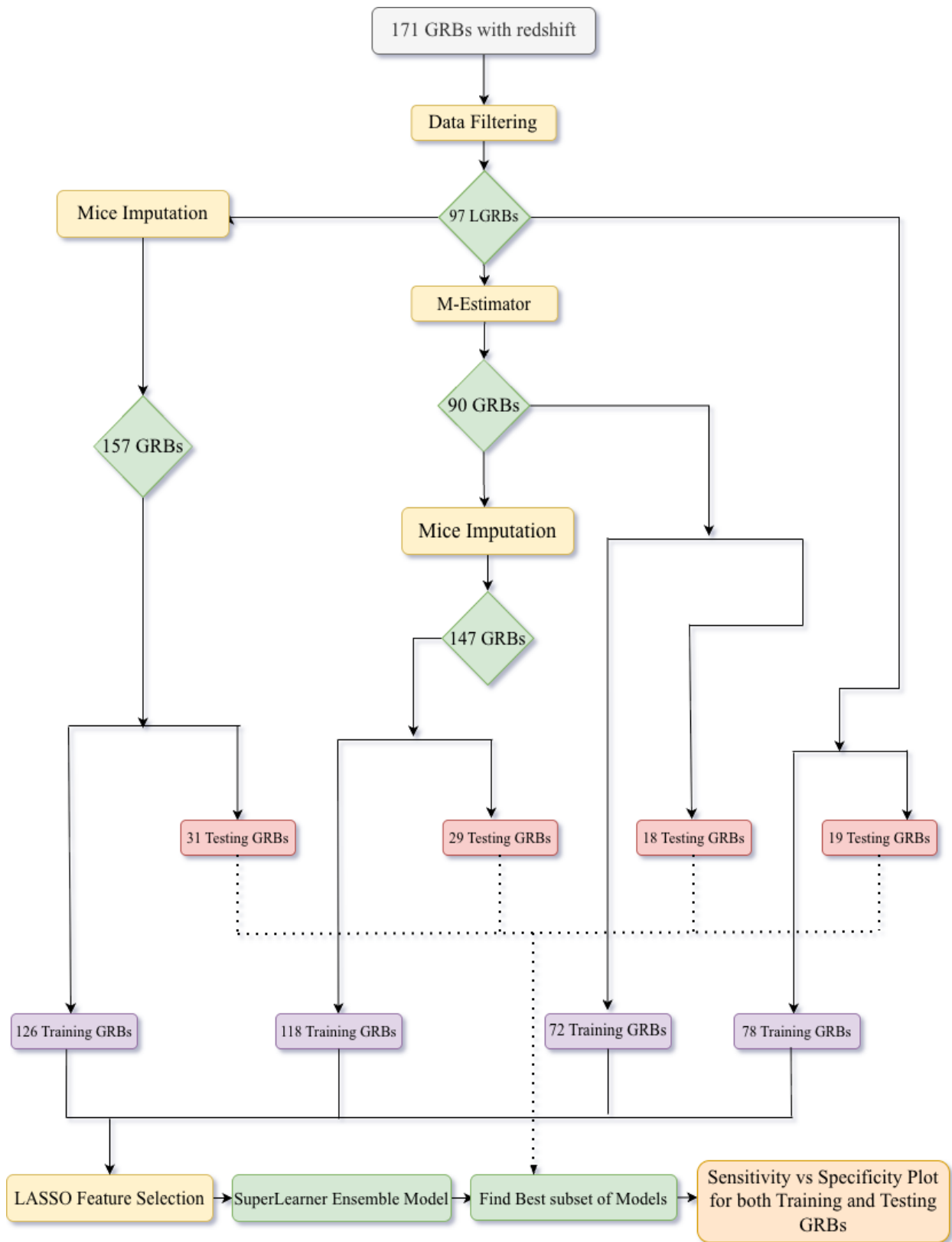


Figure 1: Flowchart detailing each pipeline step, from the initial data to the SuperLearner ensemble model. Yellow boxes show the data engineering technique applied in the pipeline. Green diamonds display the total number of GRBs after each step. Violet boxes and red boxes show the number of GRBs in the training and test sets, respectively. Green boxes highlight the steps involved in the model construction. The orange box represents the outcome of the constructed model, both applied on the test and training sets.

combinations of the variables at play were used. Because of this level of complexity, we are not yet able to interpret it.

We implemented the M-estimator method using the MASS package (Venables and Ripley, 2002) of R (R Core Team, 2022).

Figure 2 shows the distribution of the weights assigned by the M-estimator to the GRB sample. The red line denotes the weight cutoff of 0.65, and GRBs assigned weights less than the cutoff are considered outliers. We select this cutoff so that less than 5% of the data is removed as an outlier. With the 0.65 cutoff we remove 7 GRBs (4.1%) as outliers and these are GRB170714A, GRB181010A, GRB070208A, GRB070318A, GRB070419A, GRB071025A, and GRB091024. Figure 3 shows the scatter matrix plot of our data, with the outliers highlighted in green. The upper triangle of the scatter matrix plot shows the correlation between pairs of features, both for outlier and non-outlier GRBs. We also calculated the variance inflation factor (VIF) to assess multicollinearity among predictors, finding values between 1.0 and 2.59. This range, below the critical threshold of 10, suggests minimal collinearity, supporting the reliability of our M-estimator model and reliable outlier handling (Brown et al., 2009). Additionally, after outlier removal, we excluded data points where $\Delta x/x > 1$ for any feature x with error Δx . Thus, we are left with 90 GRBs.

However, we also test the cases where these M-estimator outliers are not removed, and perform a comparative measurement of our ML model’s performance with and without these outliers (see Section 4).

3.2. Data Imputation

Multivariate Imputation by Chained Equations (MICE, Schafer and Graham, 2002; van Buuren and Groothuis-Oudshoorn, 2011) is an iterative method for imputing missing values in multivariate datasets, assuming data is missing at random (MAR, (Rubin, 1976)).

This assumption is reasonable for GRB measurements, as many missing values result from observational gaps such as occultation of the event by Earth, instrumental errors or delays in follow-up observations, etc.

MICE is implemented using R, and we applied predictive mean-matching (PMM) with the *midastouch* approach (Little and Rubin, 2019). Initially, the missing values are filled with the mean of the features we are imputing. Then, the prediction is refined by training on available data, with the predictions weighted by proximity to imputed values. This methodology has already been successfully applied to active galactic nuclei (Gibson et al., 2022) and GRBs data (Bhardwaj et al., 2023; Dainotti et al., 2024a). The imputation is iterated 20 times until the imputed values are stabilized so that one iteration will not dominate. After imputation, we further exclude points where $\Delta x/x > 1$ for any feature x .

Figure 4 shows the scatter plot with MICE-imputed data shown with red dots. Figure 5 shows the distribution of missing data in our sample with red boxes highlighting GRBs with missing data points, while blue boxes indicate GRBs with complete data for a given variable.

To confirm that the imputed data aligns with the observed data’s distribution, we performed the Kolmogorov-Smirnov (KS)

test with a two-sided alternative hypothesis (Karson, 1968), with p -values averaging 0.804 across all variables. The high p -values from the test indicate no significant differences between imputed and original distributions, confirming that MICE imputation introduces no bias. Figure 6 shows the distribution of various parameters after (colored in magenta) and before (colored in blue) the application of MICE used in our analysis, with their p -value from the KS test. Here, our second division in results occurs, based on whether MICE is applied or not (see Fig. 1). After data filtering, outlier removal, and data imputation, the dataset was split into two subsets: an 80% training set for model development and a 20% test set reserved for performance evaluation.

To address class imbalance, we initially applied the Synthetic Minority Over-sampling Technique (SMOTE) (Chawla et al., 2002), which generates synthetic minority samples by interpolating between existing observations. While this approach increases minority representation and reduces overfitting compared to naive duplication, it introduced a large number of artificial samples relative to the original optical data. We used the *ubSMOTE* method implemented in the *unbalanced* R package, which added 124, 92, and 58 synthetic GRBs to the original set of 147 GRBs across $z_t = 2.0$, $z_t = 2.5$, and $z_t = 3.0$, respectively. Although we experimented with these SMOTE-augmented datasets, the resulting model performance was not promising, and the substantial injection of synthetic observations risked distorting the intrinsic distributions. For these reasons, we chose not to adopt SMOTE-based methods in our final pipeline. The results, we report in this work, therefore, correspond to the non-SMOTE analyses presented in Sec 4.

3.3. Feature Selection

Feature selection is the process where the features that are best suited to classify GRBs based on redshift, are selected. Feature selection is an essential step as it improves model interpretability, reduces dimensionality, and prevents overfitting, leading to improved ML performance in general. To select the best features for classifying high- z and low- z GRBs, we applied the Least Absolute Shrinkage and Selection Operator (LASSO) (Tibshirani, 1996), which minimizes the residual sum of squares while constraining the sum of the coefficients’ absolute values. LASSO selects a subset of predictors that best predict the response variable, z . To ensure result stability, we ran LASSO in iterations of 100, 200, 300, 500, and 1000 loops, averaging the weights for each variable. Features with weights exceeding 2% were considered the most significant and selected for model development. A 2% threshold was chosen to ensure at least 2-3 properties of the plateau emission are always selected. Reducing the threshold to 1% neither included more features nor improved prediction accuracy due to limited data. An example of the LASSO feature selection is shown in Figure 7 for a $z_t = 3.0$ with the raw dataset, raw dataset with the M-estimator, MICE-imputed dataset without M-Estimator, and MICE-imputed dataset with M-Estimator.

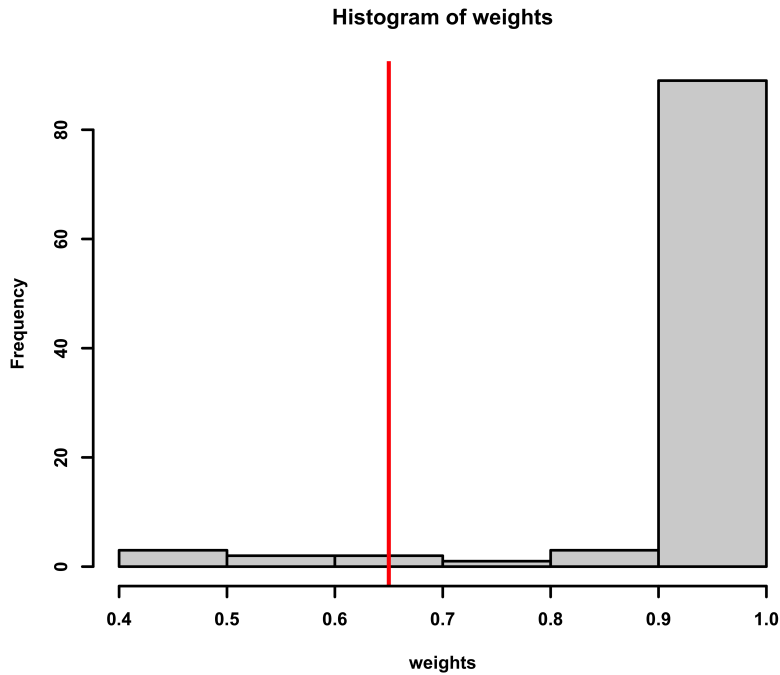


Figure 2: Distribution of weights assigned by the M-estimator to each GRB on the raw data. The red vertical line shows the cutoff line of 0.65 for the outliers. GRBs below this cutoff line are considered outliers.

3.4. Algorithms

We use a combination of parametric, semi-parametric, and non-parametric methods within the ML framework. Parametric models are efficient and easy to train, but are constrained by their predefined functional forms. Non-parametric models, on the other hand, do not assume a specific functional form, offering greater predictive power but risking overfitting and requiring large sample sizes and more computational time. Semi-parametric models combine the advantages of both parametric and non-parametric approaches, offering a balance between simplicity and flexibility. Below, we categorize the algorithms used in this study into parametric, non-parametric, and semi-parametric groups.

3.4.1. The parametric models

- Linear Model (`lm`) is one of the simplest algorithms for classification or regression, employing Ordinary Least Squares (OLS) to estimate the relationship between features and the response variable. This method assumes a linear dependency, minimizing the sum of squared differences between the predicted and actual values (Fox, 2015).
- Generalized Linear Model (`glm`) is an extension of `lm` where the relationship between features and the response is specified through a link function. This flexibility allows `glm` to accommodate various probability distributions, with parameters estimated using iterative maximum likelihood estimation (MLE). As a result, `glm` can handle distributions such as binomial, Poisson, and gamma (Nelder and Wedderburn, 1972a). In this study, we utilize the `glm` algorithm implemented in the SuperLearner package, following the work of Fox (2015).
- Lasso and Elastic-Net Regularized Generalized Linear Model (`glmnet`) is a highly efficient algorithm that computes the full regularization path for various models, including LASSO and elastic-net regularization. These models cover linear regression, logistic and multinomial regression, Poisson regression, Cox models, multiple-response Gaussian models, and grouped multinomial regression (Zou and Hastie, 2005; Friedman et al., 2010; Simon et al., 2011). By using a regularization parameter and fitting `glm` to a penalized maximum likelihood, `glmnet` effectively removes less important features, making it suitable for high-dimensional data and emphasizing highly correlated features.
- `Speedglm` and `speedlm` are faster implementations of `glm` and `lm`, respectively, designed for efficient handling of medium to large-scale datasets (Enea, 2009). By utilizing optimized Basic Linear Algebra Subprograms (BLAS) for matrix operations, these packages significantly reduce computation time while maintaining the accuracy and reliability of the standard implementations. `Speedglm` and `Speedlm` offer a practical solution for large datasets that fit into R's memory, making them valuable tools for statistical analysis in high-dimensional data contexts.
- `Bayesglm` is a Bayesian inference of `glm` and it is used to estimate coefficients, improving stability and reliability, particularly in small sample sizes or when indepen-

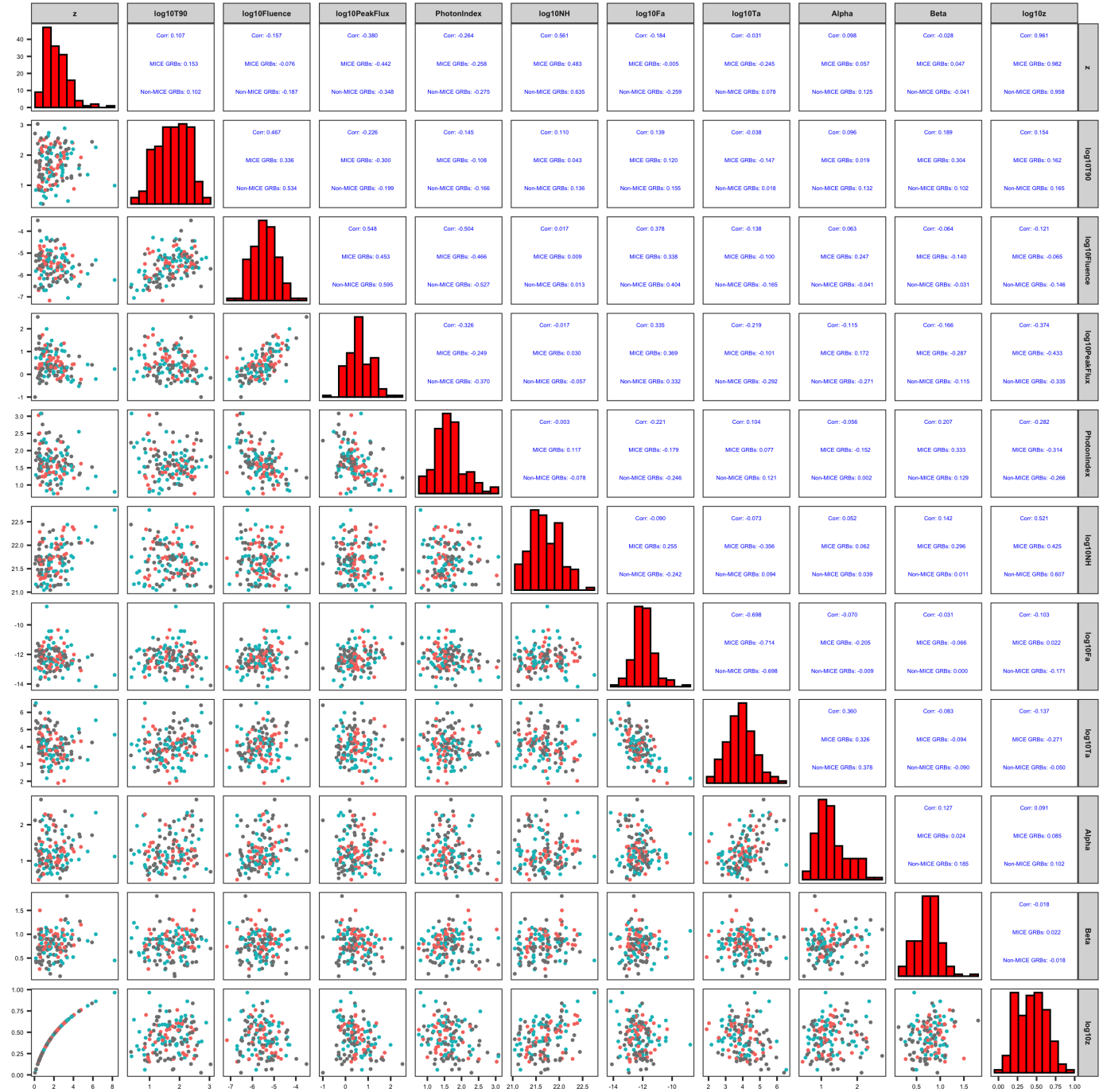


Figure 4: Scatter matrix plot for the MICE-imputed data showing the MICE-imputed data in red and the original data in cyan.

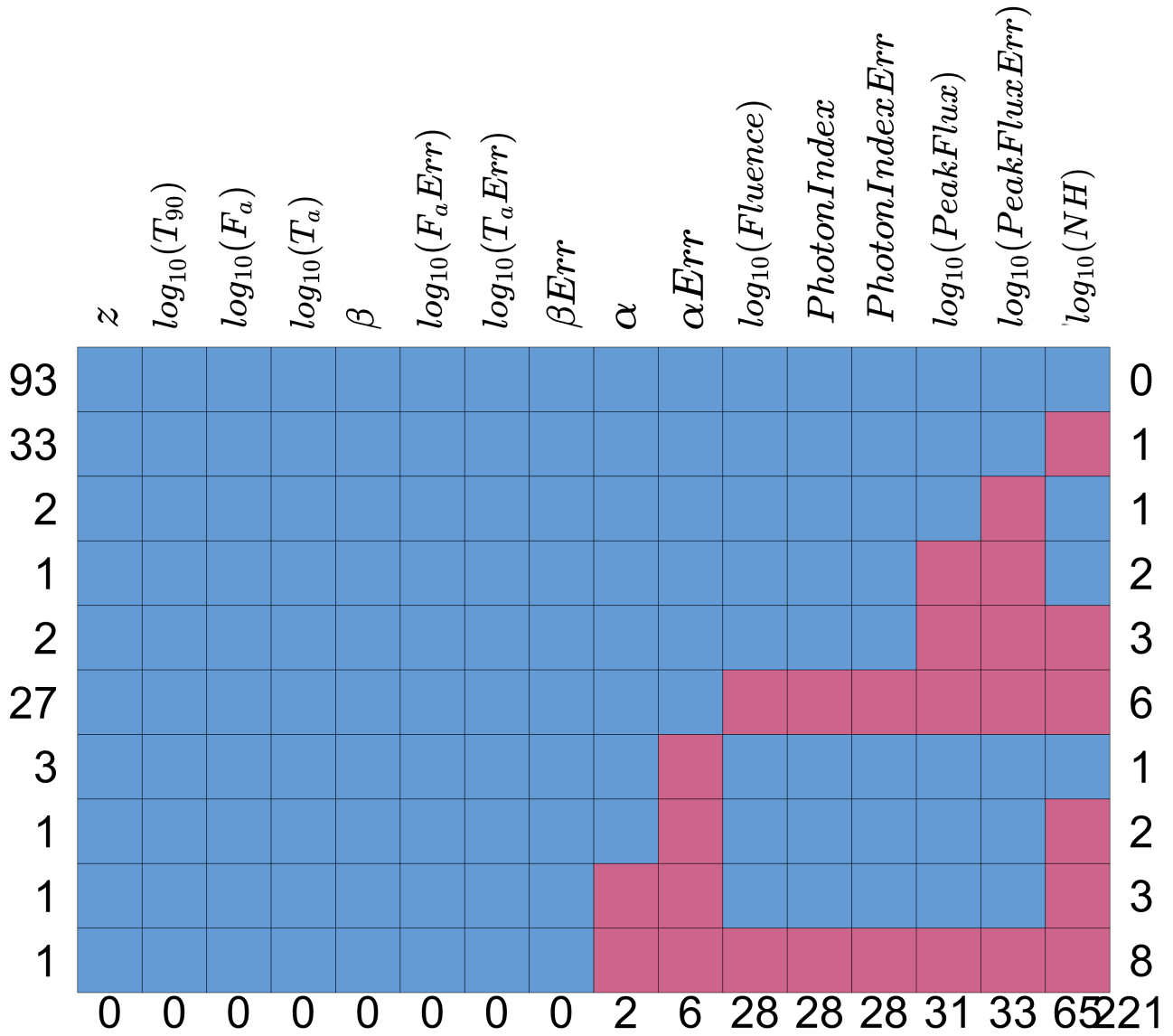


Figure 5: The distribution of missing data in our sample. Red boxes highlight GRBs with missing data points, while blue boxes indicate GRBs with complete data for a given variable, as noted on the top axis. The bottom axis enumerates the number of missing variables according to the GRB number shown on the left axis. The left axis represents the count of observations with missing data for specific features. For instance, there are 93 GRBs with complete data, 33 GRBs missing only $\log(NH)$ values, 2 GRBs missing $\log(PeakFlux_{err})$ values, and so on. The right axis indicates the number of features with missing data for each row.

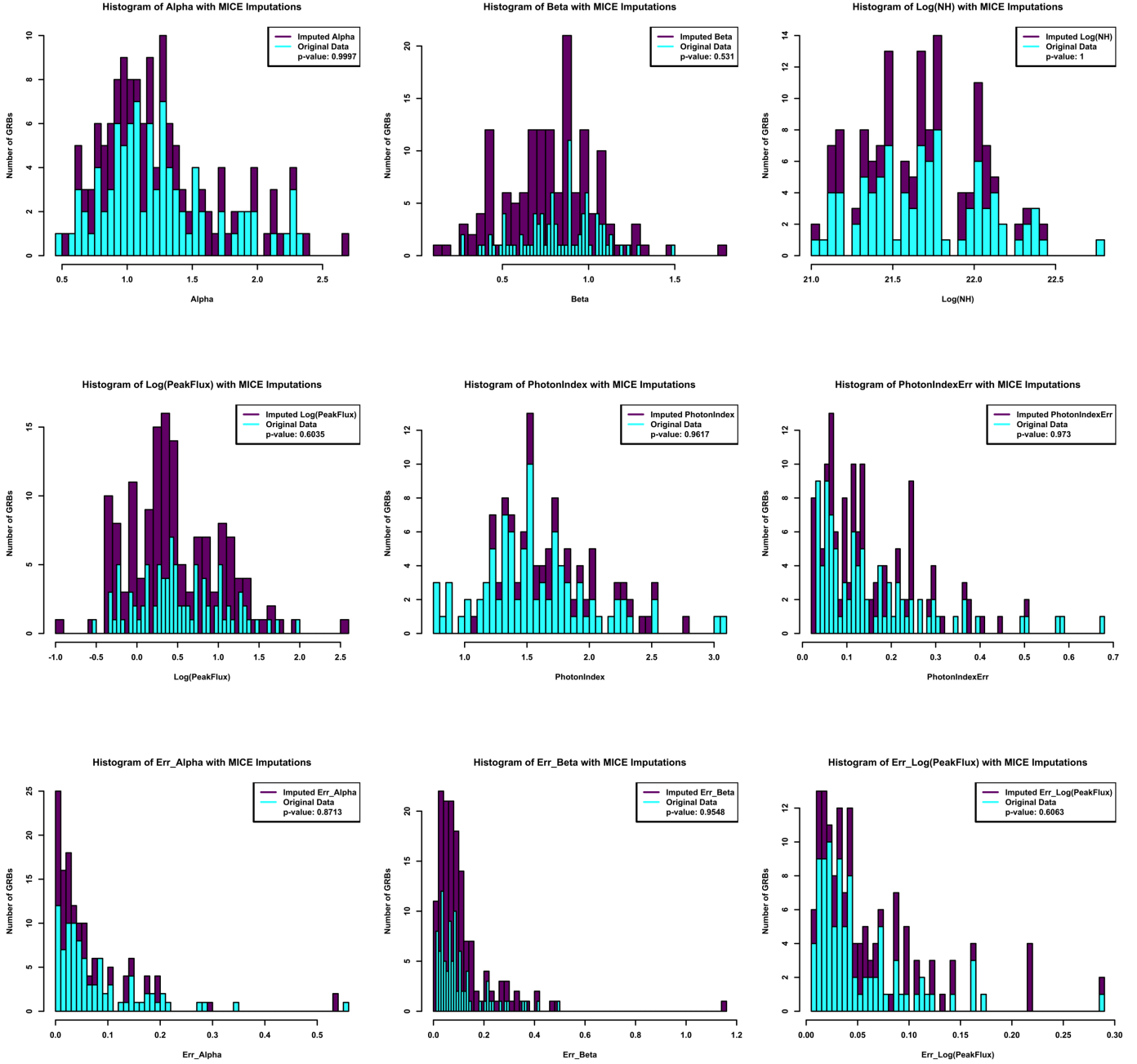


Figure 6: Distributions of α , β , Γ , $\log(\text{NH})$, $\log(\text{PeakFlux})$, PhotonIndex , $\text{Err } \log(T_{90})$, $\text{Err } \log(\text{Fluence})$, $\text{Err } \log(\text{PeakFlux})$, PhotonIndexErr , $\text{Err } \alpha$, and $\text{Err } \beta$ are shown in panels (a) to (i) with MICE imputed data in magenta and the original data in blue. The plots also show the p -value from the KS test.

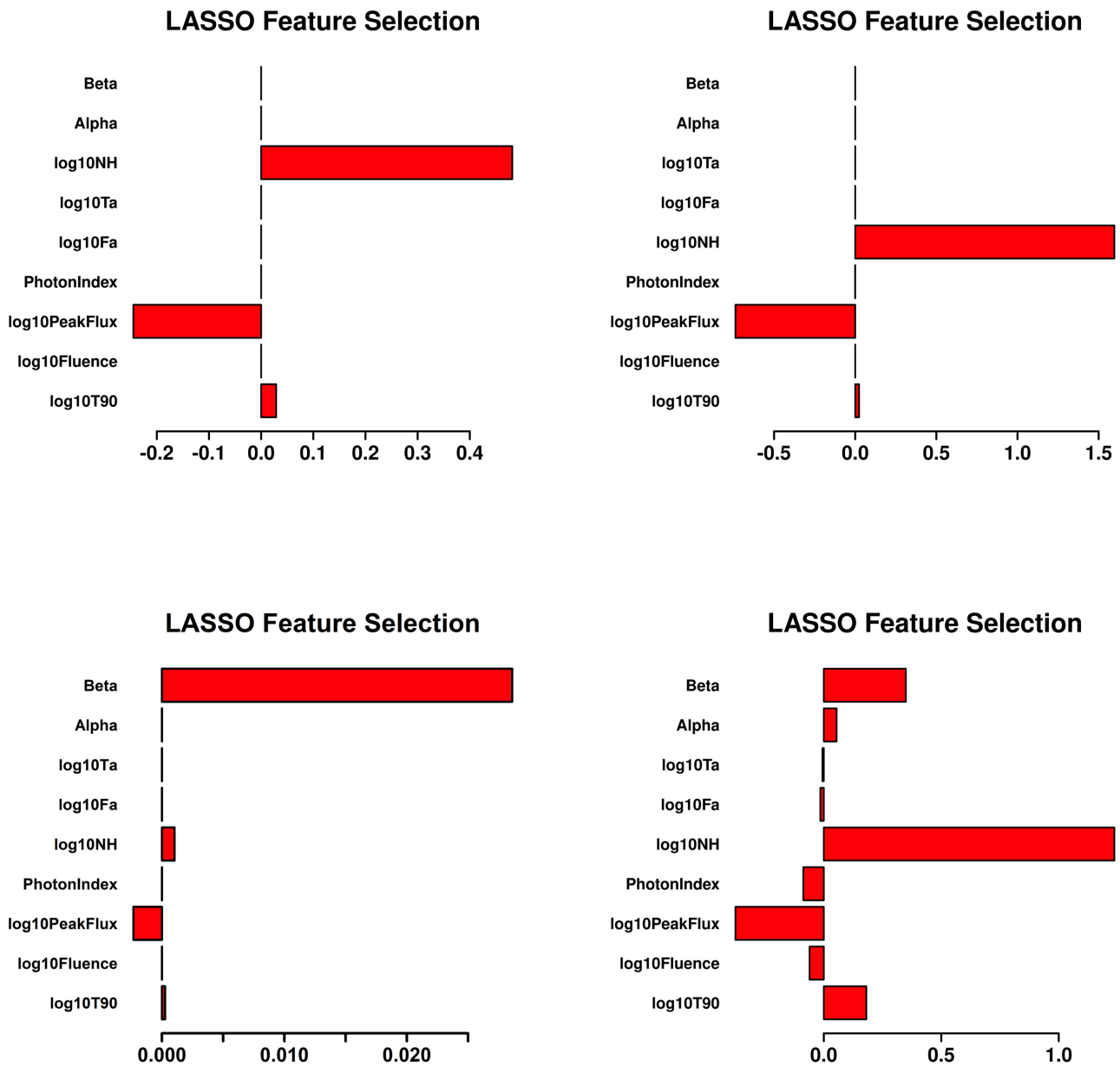


Figure 7: Weight assigned to each feature by LASSO for $z_t = 3.0$ with the raw dataset without the M-estimator (top left), the raw dataset with the M-estimator (top right), MICE-imputed dataset without M-estimator (bottom left), and MICE-imputed dataset with M-estimator (bottom right). Features with weights $> 2\%$ are selected as the best features for the classification.

dent variables are correlated (multi-collinearity). It determines the most likely estimate of the response variable given the predictors and the prior distribution of regression parameters. The `Bayesglm` method is more numerically stable than the standard `glm`, using a Student-t prior for the regression coefficients. The likelihood function for the parameters is computed, and combining this with priors produces posterior distributions from which the Maximum A Posteriori (MAP) estimates are obtained (Birnbaum, 1962; Hastie and Tibshirani, 1987, 1990; Friedman et al., 2010). This approach leads to more reliable parameter estimates, reducing overfitting and enhancing predictive performance.

- Linear Discriminant Analysis (`lda`) algorithm computes a linear combination of features to maximize class separation, assuming that the data for each class follows a normal distribution with specific mean and covariance parameters (McLachlan, 2004; Hastie et al., 2009). This makes it capable of handling high-dimensional and multicollinear data.
- Quadratic Discriminant Analysis (`qda`) is an adaptation of LDA that handles data with varying variance-covariance matrices between classes (Hastie et al., 2009), allowing for different distributions. This enables QDA to model nonlinear decision boundaries, unlike LDA.

3.4.2. The Semi-parametric models

- BigLASSO is an efficient implementation of the LASSO algorithm in R, extending traditional LASSO and elastic-net models to handle large high-dimensional datasets (Zeng and Breheny, 2017).
- Enhanced Adaptive Regression Through Hinge (`earth`) is an implementation of the Multivariate Adaptive Regression Splines (MARS) method (Friedman and Roosen, 1995), which extends linear models to capture nonlinear relationships between predictors and the response variable. Unlike traditional regression, MARS starts with a constant term and sequentially adds hinge functions or their products to adjust for changes in slope, capturing nonlinear interactions. The algorithm automatically selects important variables and interactions through a stepwise process, improving model accuracy and flexibility.

3.4.3. The non-parametric models

- Random Forest algorithm (Breiman, 2001) constructs multiple decision trees by splitting data based on randomly selected subsets of features from the training dataset (Ho, 1995). This process continues until a predefined tree depth is reached. At each node, the response variable values are averaged and used as the prediction for any data point falling within that node. The final prediction is obtained by averaging the results from all decision trees.
- Conditional Random Forest (`cforest`) algorithm extends the Random Forest model by constructing decision trees

using conditional inference (Torsten Hothorn and Zeileis, 2006), which splits trees based on significance tests that measure node purity. This prioritizes more informative features, enabling the model to capture more complex relationships (Wager and Athey, 2017).

- Ranger is an efficient implementation of the Random Forest algorithm designed for high-dimensional data, supporting ensembles of classification, regression, and survival trees. It offers faster execution and the ability to utilize highly randomized trees (ERT). ERTs stand for Extremely Randomized Trees and are constructed similarly to decision trees in Random Forest, but with randomly generated splits. The cut that minimizes prediction error is selected (Geurts et al., 2006). The increased randomness in the node-splitting process allows ERTs to reduce variance more effectively than Random Forest.
- Recursive Partitioning and Regression Trees (`rpart`) algorithm within the `caret` framework in R, which creates decision trees for classification and regression tasks (Breiman et al., 1984) by recursively partitioning the data into homogeneous subsets, until a minimum subgroup size is reached or no further improvement is possible.
- XGBoost algorithm, or extreme gradient boosting, is a scalable and distributed gradient-boosted decision tree algorithm. It provides parallel tree boosting and is widely used for regression, classification, and ranking tasks. With a more regularized model formalization, XGBoost helps prevent overfitting and outperforms single decision trees (Friedman et al., 2000, 2001; Chen and Guestrin, 2016). Unlike Random Forest, where trees operate independently, XGBoost relies on interdependent trees.
- Kernel-based k-Nearest Neighbors (`kernelKnn`) algorithm extends the traditional k-Nearest Neighbors (KNN) by applying a kernel function to assign weights to neighbors based on their distance from the query point. Unlike standard KNN, which uses Euclidean distance, `kernelKnn` constructs a mapping from the initial feature space to a higher-dimensional space (Yu et al., 2002).
- Support Vector Machine (SVM) is a supervised machine learning algorithm used for classification, regression, and outlier detection tasks (Vapnik, 1995; Cortes and Vapnik, 1995; Hastie et al., 2009). The SVM identifies the hyperplane in the multidimensional feature space that maximizes the margin between classes (e.g., high- z and low- z GRBs) while minimizing the classification error.
- Kernlab Support Vector Machine (`ksvm`) is an extension of SVM that maps input data to a higher-dimensional space using a kernel function, allowing for the handling of more complex relationships without assuming a specific parametric form (Karatzoglou et al., 2004).

3.5. SuperLearner

SuperLearner (Van der Laan et al., 2007) is an ensemble learning algorithm that combines multiple models to improve predictive performance. It uses 10-fold Cross-Validation (10fCV) to assess the model’s performance by partitioning the dataset into ten subsets, training the model on nine and testing on the remaining one, then averaging the results. Each base learner algorithm is assigned a weight based on its Root Mean Squared Error (RMSE), with the total sum of weights equaling 1 (Polley et al., 2011). We implemented SuperLearner with 10fCV repeated n times ($n = 100, 200, 300, 500, \text{ and } 1000$). Our results showed stable Area Under Curve (AUC) across runs, so we chose $n = 100$ for consistency with prior studies (Dainotti et al., 2021; Narendra et al., 2022; Dainotti et al., 2024a). We discarded models with weights below 0.05 after 100 iterations to ensure stability and enhance performance, as models with weights above this threshold showed the best prediction power. Figure 8 shows an example of the weights for a $z_t = 3.0$, where z_t is the threshold redshift. To ensure model stability, we tested SuperLearner with multiple iterations, confirming consistent results.

3.6. Metrics

This section outlines the terminology and classification metrics used to evaluate the results and the classifier’s performance. In this work, GRBs with high- z are assigned to class “1” and GRBs with low- z to class “0”. The confusion matrix, metrics, and terminology plot in Figure 9 summarizes four key definitions for these classes. The receiver operating characteristic (ROC) curve provides a visual representation of a classifier’s performance across varying classification thresholds. In this ROC space, the x-axis represents specificity, while the y-axis represents sensitivity. Each point along the ROC curve corresponds to a different decision threshold. The AUC quantifies the model’s ability to distinguish between high- z and low- z GRBs. A higher AUC value signifies better classification performance, with a maximum of 1 indicating perfect separation between the two classes. The AUC values shown in the image reflect both individual model performance and the combined effectiveness of SuperLearner. The percentage difference Δ used can be defined as the

$$\Delta = \frac{|AUC_{training} - AUC_{test}|}{\frac{(AUC_{training} + AUC_{test})}{2}}. \quad (2)$$

SuperLearner Algorithm (SLA) denotes the Superlearner algorithms with all models included and picked by the Superlearner. This notation is similar to Dainotti et al. (2025). AUC-SLA is defined as the AUC value obtained with the models selected by the Superlearner. The Least Performing Algorithms Removed (LPR) denotes the subset of Superlearner algorithms with the least performing algorithms removed from SLA. AUC-LPR is defined as the AUC value obtained with these specific models after removing the least performing ones.

4. Results

Our results are presented with the aim of providing a binary classifier for optical GRBs, which the community can freely use in the form of a web-app for follow-up observations of potentially high- z GRBs. In our analysis, high- z GRBs are equivalent to the true positives (TP, see Fig. 9) in the classifier. Thus, we are highlighting those models that achieve a high true positive rate (TPR) metric (also called the sensitivity).

Three different redshift cutoffs (z_t) of 2.0, 2.5, and 3.0 are used to assess the performance of our classifier. These cutoffs generate training sets of varying lengths, which in turn result in more or fewer training samples for high- z and low- z events. Table 1 presents the number of GRBs for each z_t . This technique helps us assess the most suitable z_t such that our classifier performs best in terms of sensitivity and AUC. For each z_t case we have used four data sets in SuperLearner: The raw dataset with and without the M-estimator, and the MICE-imputed dataset with and without the M-estimator. Thus, in total, we have twelve cases.

Table 2 summarizes the features selected by LASSO with weights $> 2\%$ for the twelve cases. Fig. 7 shows the weights assigned by LASSO to the features, for the cases of $z_t = 3.0$. Table 3 lists the top-performing algorithms chosen by SuperLearner for all twelve cases, where only models with weights above 0.05 are considered. Fig. 8 shows the weights assigned by SuperLearner for the cases of $z_t = 3.0$.

Figures 10, 11, and 12 show the specificity versus sensitivity plots for the twelve cases. Each figure consists of four rows: the first and second rows correspond to the raw data set without and with the M-estimator, respectively. The third and fourth rows represent the MICE-imputed data set without and with the M-Estimator, respectively.

In these figures, the left panels highlight the performance of the best models selected by SuperLearner, whereas the right panels showcase the outcomes after removing the least effective algorithms. Given the stochastic nature of the results, we assessed their variability and reduced randomness by performing multiple iterations of our models on the MICE-imputed data for each z_t value to ensure stable findings, specifically, by running 200, 300, 500, and 1000 iterations in addition to the original run. Furthermore, we examined the impact of large error bars by filtering out GRBs with $\Delta x/x > 1$ in the variables before applying the M-estimator. The results, as presented in Table 6, remain highly consistent with those from the initial 100-loop analysis without early $\Delta x/x$ filtering, as shown in Table 4.

Depending on the chosen model and data set, the best metric among TPR, TNR, and AUC varies. This means that a model that attains the highest TPR may not have the highest AUC. Table 5 presents the full confusion matrix for all twelve cases.

We can see that the SuperLearner model performs best in terms of TPR for $z_t = 2.0$ in the raw dataset with M-estimator (TPR = 0.741), followed by the raw dataset without M-estimator (TPR = 0.656), and the TPR values are highlighted in bold in Table 5. We can also see that for the $z_t = 2.0$, TPR falls to 0.571 (a decrease of 23%) in the MICE imputed dataset with M-estimator and further falls to 0.451 (a decrease of 39%) in

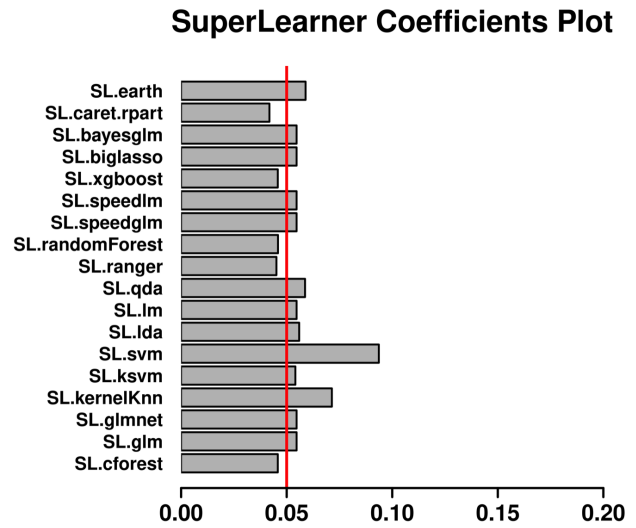
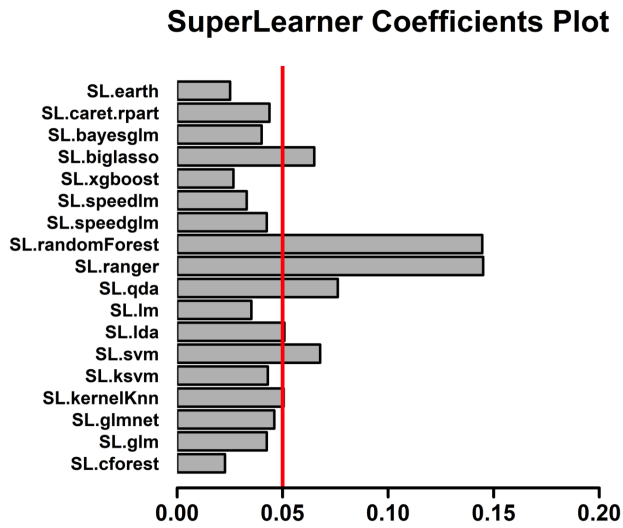
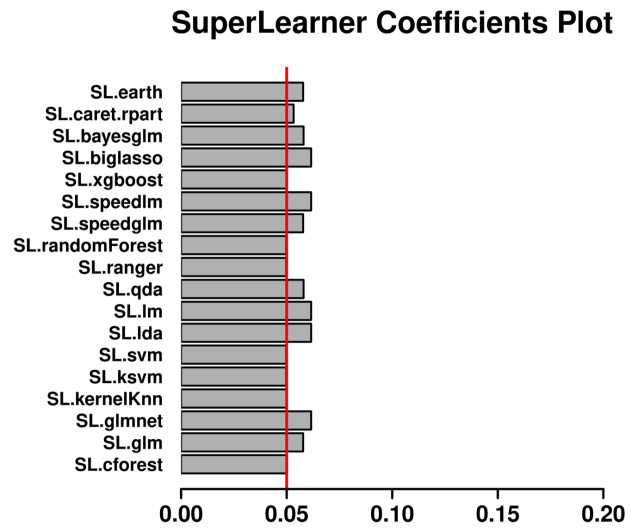
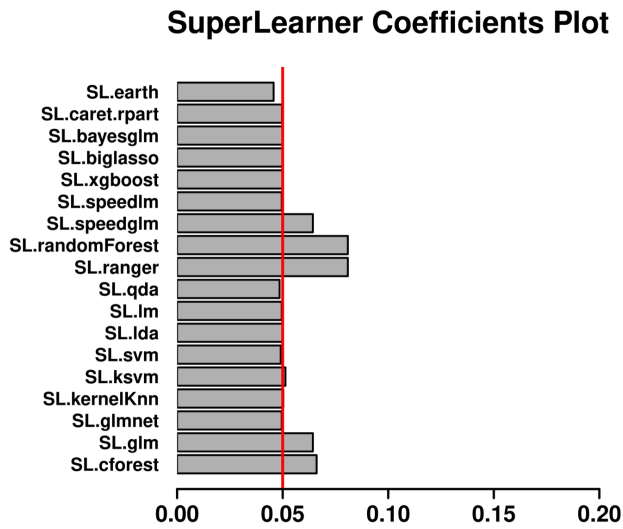


Figure 8: Weight assigned to each feature by SuperLearner for $z_T = 3.0$ with the raw dataset without the M-estimator (top left), the raw dataset with the M-estimator (top right), MICE-imputed dataset without M-estimator (bottom left), and MICE-imputed dataset with M-estimator (bottom right). Features with w

Confusion Matrix			
		Predicted Class	
		0	1
Actual Class	0	True Negative (TN) Low-z correctly predicted as low-z	False Positive (FP) Low-z incorrectly predicted as high-z
	1	False Negative (FN) High-z incorrectly predicted as low-z	True Positive (TP) High-z correctly predicted as high-z
Metrics and Terminology			
True Positive (TP) denotes the percentage of times the model correctly predicts the positive class (high-z GRB) and accurately categorizes it as positive.		True Negative (TN) denotes the percentage of data that the model correctly predicts as true negative (low-z GRB) and accurately categorizes as negative.	
False Positive (FP) denotes the percentage of data incorrectly predicted as the positive class, although they are actually the negative class.		False Negative (FN) denotes the percentage of data points incorrectly predicted as the negative class, although they belong to the positive class.	
Specificity evaluates the effectiveness of an ML model in identifying true negative instances also known as True Negative Rate (TNR)		Sensitivity evaluates the effectiveness of an ML model in identifying true positive instances also known as True Positive Rate (TPR)	
Specificity = $TN / (TN + FP)$		Sensitivity = $TP / (TP + FN)$	
Accuracy refers to the proportion of correct assessments, in our case, GRBs whose redshifts are correctly identified as both low and high-z GRBs		Precision measures the ratio of true positives (GRBs correctly classified as high-z) to the total number of positive classifications (GRBs classified as high-z).	
Accuracy = $(TP + TN) / (TP + TN + FP + FN)$		Precision = $TP / (TP + FN)$	

Figure 9: Confusion matrix in relation to our data, where the class 0 refers to low-z and 1 to high-z GRBs.

the MICE imputed dataset without M-estimator.

For $z_t = 2.5$, also, the SuperLearner model attains the highest TPR in the raw dataset with M-estimator (TPR = 0.590), followed by the raw dataset without M-estimator (TPR = 0.565). TPR drops to 0.444 (a decrease of 25%) for the MICE imputed dataset with the M-estimator and further falls to 0.289 (a decrease of 51%) for the MICE imputed dataset without the M-estimator.

Finally, for $z_t = 3.0$, the SuperLearner model attains the highest TPR on the raw dataset with M-estimator (TPR = 0.333), followed by the MICE imputed dataset with M-estimator (TPR = 0.260). TPR falls to 0.153 (a decrease of 54%) in the raw dataset without the M-estimator and further falls to 0.120 (a decrease of 64%) in the MICE data without the M-estimator. Thus, we can clearly see that in terms of TPR, SuperLearner performs the best on the raw dataset with M-estimator in the $z_t = 2.0$ cutoff.

In terms of AUC, the SuperLearner model performs the best on the raw dataset with the M-estimator across all redshift cutoffs. For $z_t = 2.0, 2.5$ and 3.0 , the AUC values are 0.841, 0.875 and 0.877, respectively. All the other cases shown in Table 4 attain AUC values lower than the aforementioned cases.

In terms of Δ , the raw dataset with M-estimator has the lowest Δ value compared to all other datasets, across all three z_t , and $z_t = 2.0$ obtains the lowest Δ value with $1\% < \Delta < 4\%$ and the highest TPR of 0.741.

Thus, based on the above results, we propose that the SuperLearner model trained with the raw dataset with M-estimator at

$z_t = 2.0$ is the best performing model. It obtains the highest TPR, the lowest Δ , and the second highest AUC.

The appendices provide a detailed breakdown of AUC performance across different z_t values (see Appendix A, Appendix B, and Appendix C, highlighting the best- and least-performing models in the training set for each threshold.

5. Discussion

In this section, we interpret the performance and implications of our optical redshift classifier, compare it with the companion X-ray classifier and earlier ML-based efforts, and describe practical tools for deployment and validation. We highlight that the optical model—trained on raw data with the M-estimator—shows the greatest sensitivity at $z_t = 2.0$, whereas the X-ray classifier is more conservative and reliable (peaking at higher z_t under imputation and class-balancing). We then examine how differing input distributions and preprocessing choices, such as the application of M-estimator, MICE, and SMOTE, affect feature selection and classification outcomes. We then validate the pipeline on an independent generalisation set, and compare classifier and regression predictions against known redshifts. The following subsections present these comparisons, methodological contrasts, web-app implementation, and validation results in detail.

Number of GRBs in the different redshift ranges		
Dataset	High- z GRBs	Low- z GRBs
$z_t = 2.0$		
Raw dataset without M-estimator:	28	50
Raw dataset with M-estimator:	29	43
MICE-imputed dataset without M-estimator:	43	83
MICE-imputed dataset with M-estimator:	39	79
$z_t = 2.5$		
Raw dataset without M-estimator:	19	59
Raw dataset with M-estimator:	18	54
MICE-imputed dataset without M-estimator:	17	109
MICE-imputed dataset with M-estimator:	22	96
$z_t = 3.0$		
Raw dataset without M-estimator:	2	64
Raw dataset with M-estimator:	5	67
MICE-imputed dataset without M-estimator:	2	124
MICE-imputed dataset with M-estimator:	10	108

Table 1: Number of high- and low- z GRBs based on the z_t of 2.0, 2.5, and 3.0 (from top to bottom of the table) across four different datasets (left column).

Features selected by LASSO in different redshift ranges with weights $> 2\%$	
Dataset	Features Selected
$z_t = 2.0$	
Raw dataset without M-estimator:	$\log(\text{PeakFlux})$, PhotonIndex , and $\log(\text{NH})$
Raw dataset with M-estimator:	$\log(\text{PeakFlux})$, PhotonIndex , and $\log(\text{NH})$
MICE-imputed dataset without M-estimator:	$\log(\text{PeakFlux})$ and $\log(\text{NH})$
MICE-imputed dataset with M-estimator:	$\log(T_{90})$, $\log(\text{PeakFlux})$, PhotonIndex , $\log(\text{NH})$, $\log(F_a)$, and $\log(T_a)$
$z_t = 2.5$	
Raw dataset without M-estimator:	$\log(T_{90})$, $\log(\text{PeakFlux})$, $\log(\text{NH})$, PhotonIndex , and β
Raw dataset with M-estimator:	$\log(\text{PeakFlux})$, $\log(\text{NH})$, PhotonIndex , and β
MICE-imputed dataset without M-estimator:	$\log(\text{NH})$ and β
MICE-imputed dataset with M-estimator:	$\log(T_{90})$, $\log(\text{PeakFlux})$, $\log(\text{Fluence})$, PhotonIndex , $\log(\text{NH})$, $\log(F_a)$, and $\log(T_a)$
$z_t = 3.0$	
Raw dataset without M-estimator:	$\log(T_{90})$, $\log(\text{PeakFlux})$, and $\log(\text{NH})$
Raw dataset with M-estimator:	$\log(T_{90})$, $\log(\text{PeakFlux})$, and $\log(\text{NH})$
MICE-imputed dataset without M-estimator:	$\log(\text{PeakFlux})$, $\log(\text{NH})$ and β
MICE-imputed dataset with M-estimator:	$\log(T_{90})$, $\log(\text{PeakFlux})$, $\log(\text{Fluence})$, PhotonIndex , $\log(\text{NH})$, $\log(F_a)$, $\log(T_a)$, α , and β

Table 2: Features selected by LASSO with weights $> 2\%$ for z_t of 2.0, 2.5, 3.0 (top to bottom panels) across four different datasets (left column).

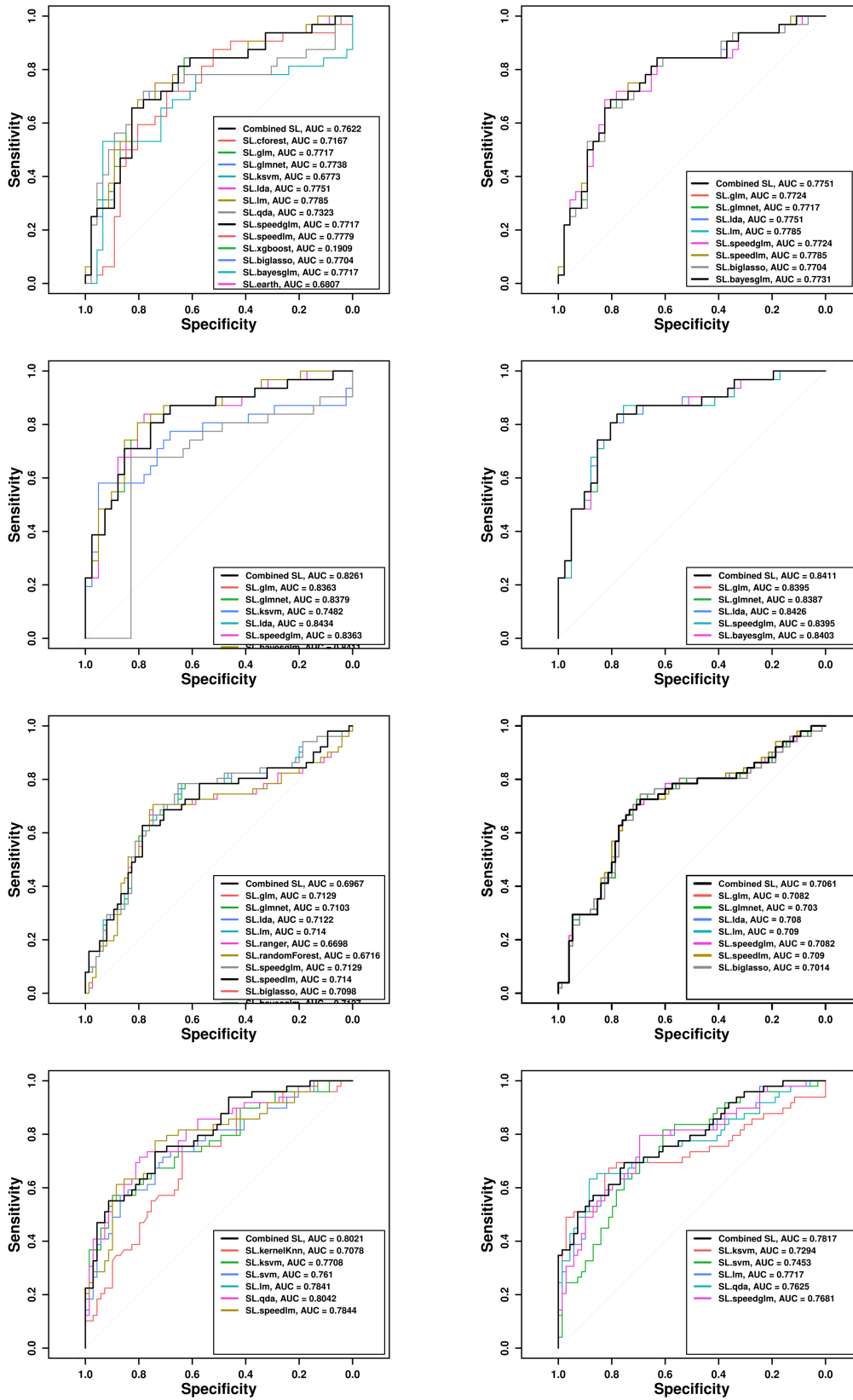


Figure 10: For $z_T = 2.0$. Top row: raw without M-estimator. Second row: raw with M-estimator. Third row: MICE-imputed without M-estimator. Bottom row: MICE-imputed with M-estimator. First column: ROC-AUC curve with best algorithms chosen by SuperLearner with weights > 0.05 in each dataset. Top right: ROC-AUC curve without 'caret.rpart'. Second right: ROC-AUC curve without 'caret.rpart'. Third right: ROC-AUC curve without 'kernelKnn' and 'xgboost'. Bottom right: ROC-AUC curve without 'kernelKnn', 'ksvm', 'svm', and 'qda'.

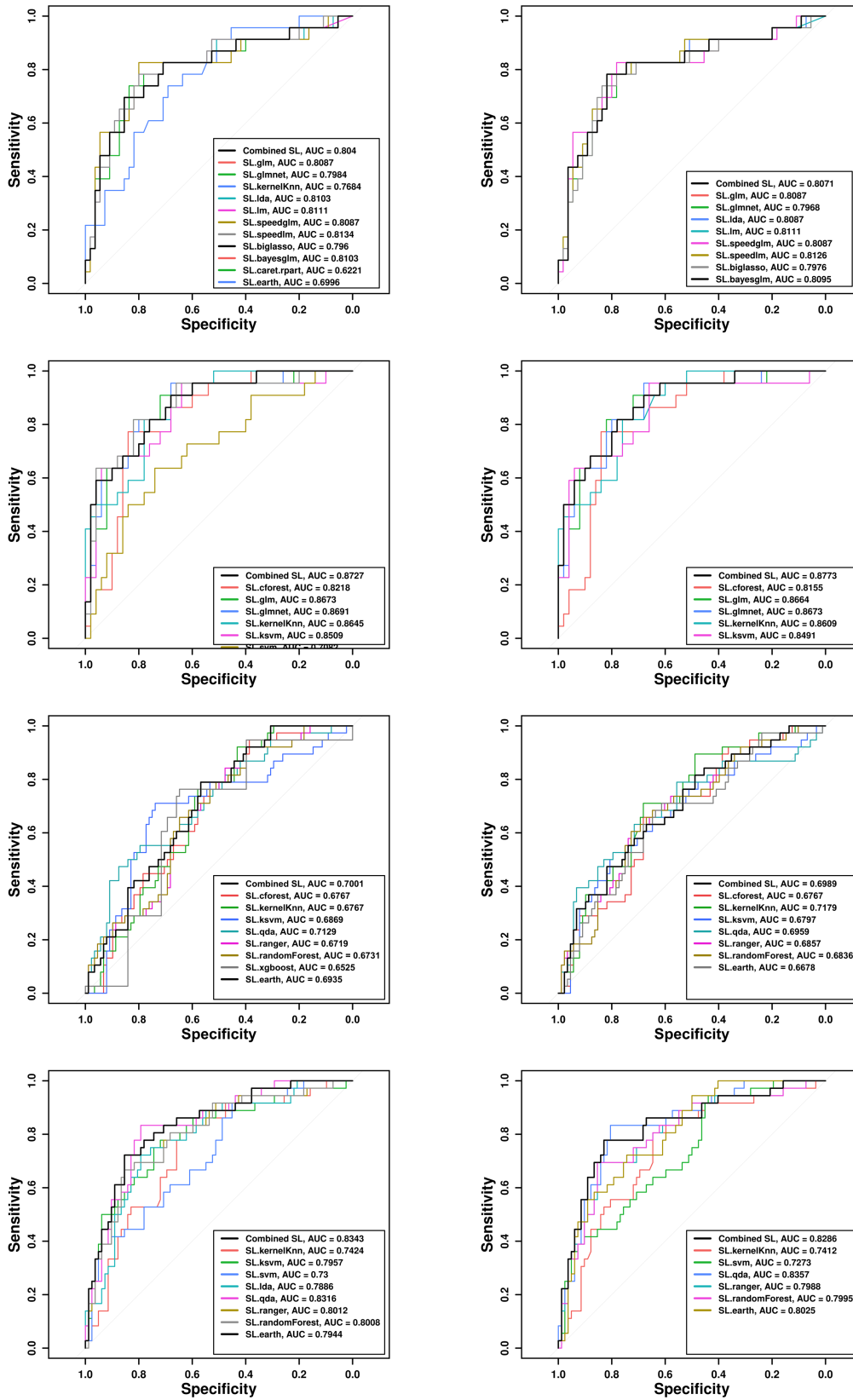


Figure 11: For $z_t = 2.5$. Top row: raw without M-estimator. Second row: raw with M-estimator. Third row: MICE-imputed without M-estimator. Bottom row: MICE-imputed with M-estimator. First column: ROC-AUC curve with best algorithms chosen by SuperLearner with weights > 0.05 in each dataset. Top right: ROC-AUC curve without 'caret.rpart'. Second right: ROC-AUC curve without 'svm' and 'xgboost'. Third right: ROC-AUC curve without 'kernelKnn' and 'xgboost'. Bottom right: ROC-AUC curve without 'svm', 'qda', 'xgboost', and 'earth'.

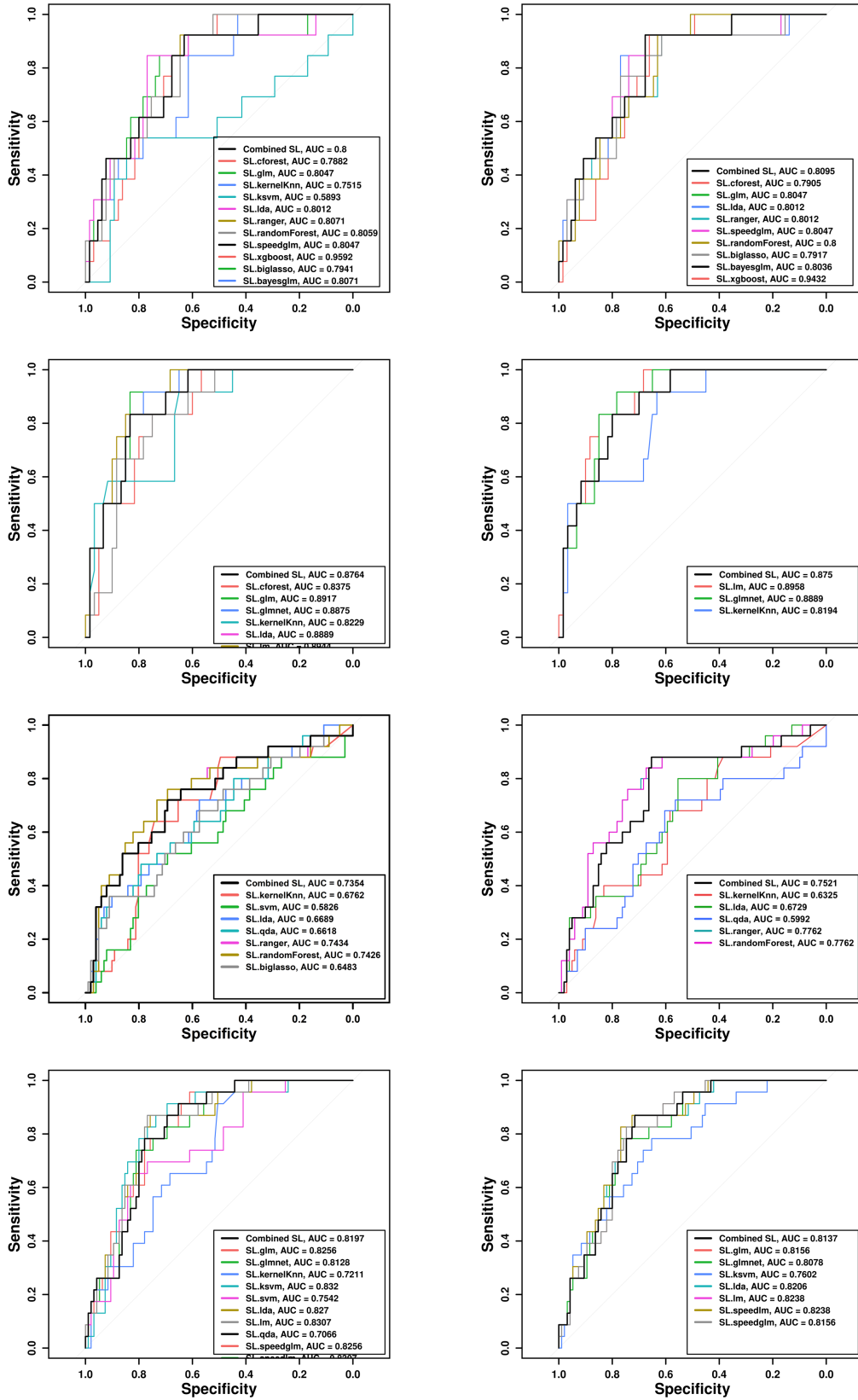


Figure 12: For $z_r = 3.0$. Top row: raw without M-estimator. Second row: raw with M-estimator. Third row: MICE-imputed without M-estimator. Bottom row: MICE-imputed with M-estimator. First column: ROC-AUC curve with best algorithms chosen by SuperLearner with weights > 0.05 in each dataset. Top right: ROC-AUC curve without 'ksvm' and 'svm'. Second right: ROC-AUC curve without 'caret.rpart'. Third right: ROC-AUC curve without 'ksvm'. Bottom right: ROC-AUC curve without 'ksvm' and 'svm'.

Data sets and Algorithms selected by the Superlearner in the z_t ranges with weights > 0.05	
Dataset	Algorithms Selected
$z_t = 2.0$	
Raw dataset without M-estimator:	log(peak flux), PhotonIndex, log(NH)
Raw dataset with M-estimator:	log(peak flux), PhotonIndex, log(NH)
MICE-imputed dataset without M-estimator:	log(peak flux), log(NH)
MICE-imputed dataset with M-estimator:	log T_{90} , log(peak flux), PhotonIndex, log(NH), log(F_a), log(T_a)
$z_t = 2.5$	
Raw dataset without M-estimator:	log T_{90} , log(peak flux), PhotonIndex, log(NH), β
Raw dataset with M-estimator:	log(peak flux), PhotonIndex, log(NH), β
MICE-imputed dataset without M-estimator:	log(NH), β
MICE-imputed dataset with M-estimator:	log T_{90} , log(Fluence), log(peak flux), PhotonIndex, log(NH), log(F_a), log(T_a)
$z_t = 3.0$	
Raw dataset without M-estimator:	log T_{90} , log(peak flux), log(NH)
Raw dataset with M-estimator:	log T_{90} , log(peak flux), log(NH)
MICE-imputed dataset without M-estimator:	log(peak flux), log(NH), β
MICE-imputed dataset with M-estimator:	log T_{90} , log(Fluence), log(peak flux), PhotonIndex, log(NH), log(F_a), log(T_a), α , β

Table 3: Algorithms selected by SuperLearner with weights > 0.05 for z_t of 2.0, 2.5, 3.0, and 3.5 (from top to bottom panel) across four different datasets (left column).

AUC for SuperLearner for training and test sets					
Dataset	AUC - SLA	Δ_{SLA} (%)	AUC - LPR	Δ_{LPR} (%)	
$z_t = 2.0$					
Raw dataset without M-estimator:	0.762, 0.711	7 %	0.775, 0.722	7 %	
Raw dataset with M-estimator:	0.826, 0.837	1 %	0.841, 0.812	4 %	
MICE-imputed without M-estimator:	0.696, 0.606	14 %	0.706, 0.645	9 %	
MICE-imputed with M-estimator:	0.802, 0.692	15 %	0.781, 0.649	18 %	
$z_t = 2.5$					
Raw dataset without M-estimator:	0.804, 0.722	11 %	0.807, 0.744	8 %	
Raw dataset with M-estimator:	0.872, 0.753	15 %	0.877, 0.790	10 %	
MICE-imputed without M-estimator:	0.700, 0.581	18 %	0.698, 0.652	7 %	
MICE-imputed with M-estimator:	0.834, 0.731	13 %	0.828, 0.700	17 %	
$z_t = 3.0$					
Raw dataset without M-estimator:	0.800, 0.833	4 %	0.809, 0.833	3 %	
Raw dataset with M-estimator:	0.876, 0.833	5 %	0.875, 0.833	5 %	
MICE-imputed without M-estimator:	0.735, 0.860	16 %	0.752, 0.866	14 %	
MICE-imputed with M-estimator:	0.819, 0.826	1 %	0.813, 0.789	3 %	

Table 4: AUC - SLA is the AUC from the SuperLearner selected algorithms, AUC - LPR is the AUC without the least-performing models, and AUC - BPM is the AUC with the best-performing models. The second, fourth, and sixth columns contain the training and test AUC values for each z_t . The third, fifth, and seventh columns show the percentage difference between the training and testing AUC. The percentage difference here is calculated as the absolute deviation of the training vs. the test set divided by their mean. These values are already rounded to the third significant digit from our analysis.

5.1. Lyman- α Break, Dropout Techniques, and the Scope of the Present Analysis

The standard dropout (Lyman-break) technique is the canonical method used to identify high-redshift galaxies and GRB af-

terglows using broadband photometry. It relies on the strong absorption by neutral hydrogen in the intergalactic medium at wavelengths shorter than (i.e., blueward of) the Lyman- α transition at 1216 Å. For a source at sufficiently high redshift, this

Confusion Matrix for the several datasets including TNR and TNR					
$z_t = 2.0$					
TNR and TPR	Raw without M-estimator		Raw without M-estimator - algos removed	TNR and TPR	
0.826	38	12	38	11	0.826
0.625	8	2	8	21	0.656
TNR and TPR	Raw with M-estimator		Raw with M-estimator - algos removed	TNR and TPR	
0.829	34	9	33	8	0.804
0.709	7	22	8	23	0.741
TNR and TPR	MICE without M-estimator		MICE without M-estimator - algos removed	TNR and TPR	
0.786	59	24	60	28	0.800
0.529	16	27	15	23	0.451
TNR and TPR	MICE with M-estimator		MICE with M-estimator - algos removed	TNR and TPR	
0.840	58	21	60	21	0.869
0.571	11	28	9	28	0.571
$z_t = 2.5$					
TNR and TPR	Raw without M-estimator		Raw without M-estimator - algos removed	TNR and TPR	
0.890	49	10	48	10	0.872
0.565	6	13	7	13	0.565
TNR and TPR	Raw with M-estimator		Raw with M-estimator - algos removed	TNR and TPR	
0.900	45	9	47	9	0.940
0.590	5	13	3	13	0.590
TNR and TPR	MICE without M-estimator		MICE without M-estimator - algos removed	TNR and TPR	
0.897	79	30	82	27	0.931
0.210	9	8	6	11	0.289
TNR and TPR	MICE with M-estimator		MICE with M-estimator - algos removed	TNR and TPR	
0.926	76	20	75	20	0.914
0.444	6	16	7	16	0.444
$z_t = 3.0$					
TNR and TPR	Raw without M-estimator		Raw without M-estimator - algos removed	TNR and TPR	
0.984	64	12	63	11	0.969
0.076	1	1	2	2	0.153
TNR and TPR	Raw with M-estimator		Raw with M-estimator - algos removed	TNR and TPR	
0.983	59	8	59	8	0.983
0.333	1	4	1	4	0.333
TNR and TPR	MICE without M-estimator		MICE without M-estimator - algos removed	TNR and TPR	
0.980	99	25	98	22	0.970
0.000	2	0	3	3	0.120
TNR and TPR	MICE with M-estimator		MICE with M-estimator - algos removed	TNR and TPR	
0.957	91	17	90	17	0.947
0.260	4	6	5	6	0.260

Table 5: Confusion matrices for the training set of each dataset with their respective TNR (every first row) and TPR (every second row).

absorption produces a sharp suppression of flux in observer-frame bands located at wavelengths shorter than the redshifted $Ly\alpha$ transition, while redder bands remain largely unaffected. This wavelength-dependent discontinuity leads to characteristic non-detections (“dropouts”) in specific filters and underpins the majority of high-redshift galaxy surveys and early GRB afterglow redshift identifications.

Works by Prochaska et al. (2007, 2008) have demonstrated both the effectiveness and the limitations of applying dropout-based techniques to GRB afterglows. In particular, these studies showed that reliable redshift identification through afterglow photometry or spectroscopy requires early, band-resolved optical observations that preserve wavelength-dependent information, and that a substantial fraction of GRBs are optically faint or “dark” due to dust extinction in their host galaxies or ab-

sorption at high redshift. They further established that, when such multiband information is unavailable, redshift recovery must instead rely on host-galaxy identification and late-time spectroscopy rather than on dropout-based afterglow methods, a conclusion reinforced by subsequent GRB host-galaxy surveys (Perley et al., 2009, 2013).

The optical plateau sample employed in this work does not satisfy the observational requirements needed to apply the Lyman- α break technique. The plateau light curves are constructed from highly heterogeneous observations obtained with Swift/UVOT and more than 450 ground-based facilities, often using different filters, unfiltered imaging, and non-uniform observing cadences. To enable a statistically meaningful ensemble analysis that present plateau emission fitable within a single plateau fluxes are homogenized by rescaling to a common R-band reference

Loop for each z_t repeated twice for the MICE imputed data										
Run	100 loops		200 loops		300 loops		500 loops		1000 loops	
	Training Test		Training Test		Training Test		Training Test		Training Test	
$z_t = 2.0$										
1	0.7972	0.6923	0.8007	0.6923	0.8048	0.7067	0.8039	0.7115	0.8098	0.7067
2	0.8045	0.7115	0.8137	0.7067	0.8007	0.6971	0.8001	0.6971	0.8027	0.6982
$z_t = 2.5$										
1	0.8283	0.7421	0.8367	0.7368	0.8279	0.7001	0.8296	0.6895	0.8404	0.7474
2	0.8313	0.7316	0.7913	0.5737	0.8313	0.7211	0.8316	0.7211	0.7984	0.6737
$z_t = 3.0$										
1	0.8252	0.8116	0.8096	0.7899	0.8101	0.7826	0.8243	0.8043	0.8119	0.7826
2	0.8261	0.8333	0.8275	0.8333	0.8146	0.7754	0.8092	0.7681	0.8316	0.8333

Table 6: Combined training and testing data AUC scores with MICE-imputed dataset for $z_t = 2.0, 2.5, 3.0,$ and 3.5 (from top to bottom). The left value in each loop column shows the AUC value for the training dataset, while the right value in each loop column shows the AUC value for the testing dataset.

using the observed or inferred optical spectral index β (Dainotti et al., 2022a).

By construction, this R-band rescaling removes the original wavelength-dependent information into an effective single-band representation. As a direct consequence, any filter-specific signature—most notably the supereverages the observer-frame properties of optical plateau emission, along with due to intergalactic absorption—cannot be reconstructed a posteriori without reverting to a full multi-wavelength analysis. Such an approach would require restricting the analysis to a substantially smaller subset of GRBs, which present plateau emission fittable within one filter, further reducing an already limited sample.

5.2. The Model Performance

The performance of the classifier does not rely on the identification of specific spectral features, such as the Lyman- α break, but instead reflects correlations among observables that encode redshift information at a population level. In particular, the model exploits the observer frame properties of the optical plateau emission together with prompt gamma-ray characteristics. When considered jointly, these variables exhibit statistical patterns across the GRB population that the classifier can learn even in the absence of explicit spectral diagnostics. This behaviour indicates that the model captures population-level relationships present in the data rather than relying on individual event-specific signatures. We emphasize that the inferred redshift estimates are inherently probabilistic and should be interpreted as statistical indicators rather than precise measurements. As such, they are not intended to replace spectroscopic or host-galaxy redshift determinations, but to provide complementary information on the redshift distributions of GRBs that lack secure measurements.

5.3. Comparing parameters of Optical and X-Ray Samples

Our optical classifier and the X-ray classifier presented in Dainotti et al. (2025) are constructed from distinct but structurally similar datasets, both drawn from *Swift*-detected LGRBs but differing in observational wavelength, sample size, and data processing strategies.

The X-ray classifier uses a larger sample of 251 GRBs with well-characterized plateau phases in the X-ray band, primarily from the BAT and XRT instruments onboard *Swift*. It includes eleven features spanning the prompt, plateau, and afterglow phases. In contrast, the optical classifier relies on 171 GRBs with identified optical plateaus, compiled from both UVOT and over 455 ground-based telescopes. It uses a subset of ten comparable features, but restricted to GRBs with optical afterglow and plateau measurements. While both datasets share core variables (e.g., T_{90} , F_a , T_a , NH), the X-ray sample includes Γ , the spectral index for the XRT detection of the burst source obtained from an automated time-averaged spectral fit of the Photon Counting (PC) mode data. If the PC-mode data are not available then the Window Timing mode data are used. This variable is not available in the optical dataset.

In terms of preprocessing, both classifiers analyze four main data variants: raw data with and without the M-estimator, and MICE-imputed data with and without the M-estimator. However, only the X-ray model additionally uses a SMOTE-balanced dataset to counter class imbalance. The optical model avoids SMOTE to preserve physically realistic distributions, as over-sampling can distort early-time optical light curve properties. Finally, MICE imputation has differing effects: the X-ray classifier benefits from imputed data, while the optical classifier exhibits lower performance with the imputed data. This could be due to greater variability and observational uncertainty in the optical features.

We also compare the input parameters for the two classifiers with a scatter matrix plot in Fig. 13 displaying the comparison between the four parameters (F_a , T_a , α , β). The other parameters, such as the NH and T_{90} , remain the same, and thus we do not show their comparison. It can be seen that most input parameters, T_a , α , and β , are equally distributed around the equality line. However, in the F_a plot (bottom left), we can see that the $F_{a,x}$ is higher than the $F_{a,opt}$ by several orders of magnitude.

Furthermore, Fig 14 shows the distribution of difference in the input parameters (F_a , T_a , α , β) of the X-ray and optical classifier. These distributions give an indication of how different the input parameters are. The largest spread is seen in the

$\log_{10}F_{a,x} - \log_{10}F_{a,opt}$ distribution, where it is skewed towards the positive values. The mean and standard deviation of this distribution are 1.62 and 0.89, respectively. This is $> 1\sigma$ away from zero. These results are aligned with the correlation plot of F_a in Fig. 13 with $F_{a,x}$ being higher than $F_{a,opt}$. The rest of the differences of the distributions are normally distributed around 0, namely the mean of all these distributions is within 1σ deviation from zero. This test shows that F_a could be one of the input parameters that causes the difference in the optical and X-ray classifier results to detect high- z GRBs.

5.4. Comparison with Similar X-Ray Analysis

The objective of both our optical classifier and the X-ray classifier presented in Dainotti et al. (2025) is to support high- z GRB identification for timely follow-up observations using ensemble learning across various redshift thresholds and data treatments. While following a similar methodology, the classifiers show distinct performance patterns and sensitivities.

The optical model achieves its best performance at $z_t = 2.0$ using the raw dataset with the M-estimator, reaching a TPR of 0.741, an AUC of 0.841, and a deviation between training and test sets ($1\% < \Delta < 4\%$). In contrast, the X-ray classifier attains its highest AUC (0.85) at $z_t = 3.5$ using MICE-imputed data, with a Δ ($3\% < \Delta < 15\%$), albeit with a lower TPR of 0.583. These findings suggest that the optical classifier is more sensitive to high- z events, while the X-ray model is more conservative and balanced across classes.

The optical classifier’s performance declines significantly with MICE imputation - a 39% TPR drop at $z_t = 2.0$ - suggesting that key redshift-linked patterns in early-time optical data may be diminished by imputation. In contrast, the X-ray classifier benefits from such treatments, with MICE and SMOTE datasets yielding better or more stable results, likely due to smoother temporal and spectral features in X-ray afterglows.

Feature selection via LASSO shows a partial but meaningful overlap between the optical and X-ray classifiers. In both cases, $\log(\text{PeakFlux})$, PhotonIndex , and $\log(\text{NH})$ are consistently selected, indicating that these parameters carry reliable redshift-discriminatory power independent of wavelength regime.

For the optical classifier, however, the set of selected features varies more noticeably across different training subsets. Depending on the specific dataset or redshift threshold, LASSO intermittently selects $\log(T_{90})$, $\log(F_a)$, $\log(T_a)$, and β , suggesting that the optical model is more sensitive to sampling fluctuations and to correlations that are weaker or less stable across the sample.

In contrast, the X-ray classifier exhibits a more stable feature-selection pattern. Across different redshift thresholds and imputation settings, LASSO consistently retains $\log(F_a)$ and $\log(T_a)$, with β and Γ appearing only occasionally. This relative stability refers to the fact that the X-ray model repeatedly selects the same core set of features regardless of dataset variations, implying that X-ray temporal structure provides stronger or more uniformly expressed correlations with redshift in the training sample.

Overall, while both classifiers share a subset of key predictors, the optical model displays greater variability in selected

features, whereas the X-ray model shows a more reliable and reproducible selection profile across methodological choices.

Our optical classifier’s sensitivity aligns with expectations that early-time flux and spectral behavior in optical bands can be informative for redshift estimation, despite observational scatter. The reduced effectiveness of imputation suggests that intrinsic GRB-to-GRB variation or measurement uncertainties in optical light curves are significant. Meanwhile, the reliability of the X-ray model under imputation and balancing supports the idea that X-ray properties—such as duration, absorption, and photon index—offer more consistent proxies for redshift classification, particularly in the X-ray afterglow phase.

Thus, our optical classifier at $z_t = 2.0$ using raw data with the M-estimator offers the best performance in terms of sensitivity and generalization. The X-ray classifier, particularly at $z_t = 3.5$, provides a more stable and balanced model, better suited when broader coverage is needed. These findings motivate future strategies that integrate optical and X-ray classifiers to improve redshift estimation reliability and coverage.

We also note that ML models that used only prompt emission properties, besides $\log(\text{NH})$ for the classifier, are at $z_t = 2$ for the raw data with and without M-estimator. Thus, in this regard, we would not even need the properties of the plateau emission to classify between low- z and high- z GRBs. This will give a substantial advantage for a fast follow-up.

5.5. Comparison with earlier results

We also compare our optical classifier with previous ML models that used prompt emission and X-ray features to estimate GRB redshifts, particularly the works of Morgan et al. (2012) and Ukwatta et al. (2016); Aldowma and Razzaque (2024). When evaluated on an independent generalisation sample, our full SuperLearner ensemble achieves an AUC of 0.9338, corresponding to an improvement of approximately 10 – 15% in discrimination power relative to the AUC values ($\sim 0.8 - 0.85$) reported for the prompt-emission-based high-redshift GRB classifier of Aldowma and Razzaque (2024). These earlier studies used parameters such as T_{90} , Photon Index, and Peak Flux derived from prompt gamma-ray or early X-ray emission, and trained Random Forest classifiers to identify high- z GRBs. Morgan et al. (2012), using a dataset of 135 GRBs without a separate test set, reported an AUC of 84%. Similarly, 80% sensitivity and 89% AUC, but sample at $z_t = 4.0$ and achieved a sensitivity of 80% and an AUC of 89%, but with no separate test set for validation.

Our optical classifier improves upon these works in several key ways. First, our methodology incorporates an 80/20 train-test split across multiple redshift thresholds ($z_t = 2.0, 2.5,$ and 3.0), ensuring model generalization is properly evaluated. Second, we evaluate the classifier performance across four dataset configurations (raw dataset without M-estimator, raw dataset with M-estimator, MICE-imputed dataset without M-estimator, and MICE-imputed dataset with M-estimator), using repeated iterations. Our best-performing model trained on raw optical data with the M-estimator at $z_t = 2.0$ achieves a TPR of 0.741 and an AUC of 0.841.

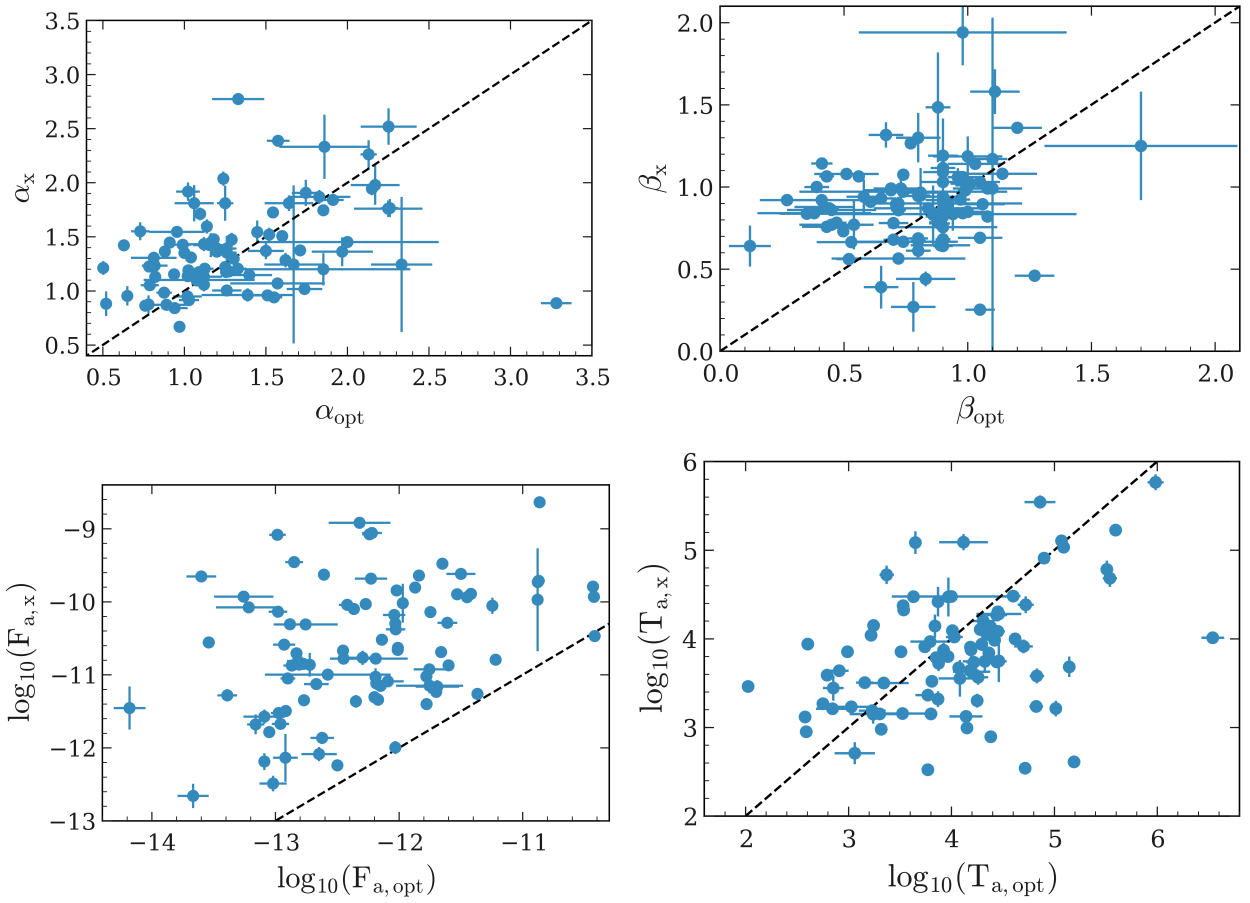


Figure 13: Optical vs X-ray classifier input parameter correlation plots. The black dashed line is the 1:1 correlation line.

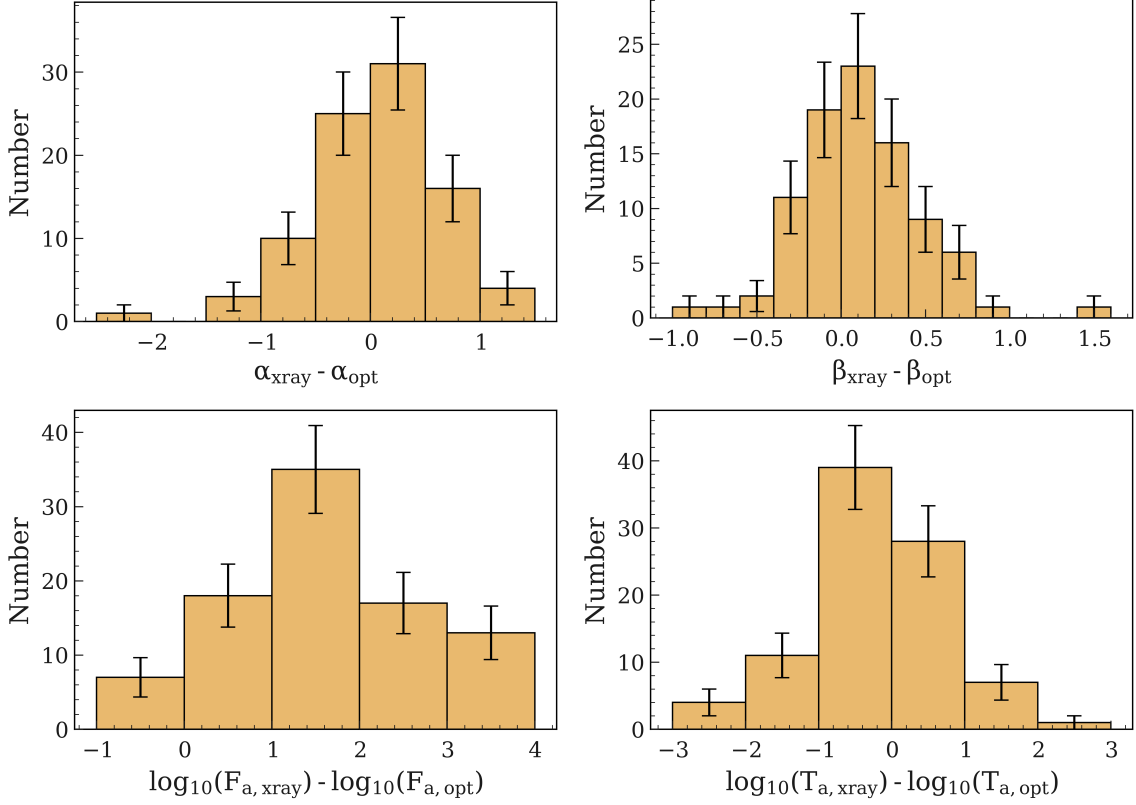


Figure 14: Optical vs X-ray classifier input parameter histograms. The histograms are constructed to compare the difference between the two parameter sets. We subtract the optical parameters from the X-ray parameters. The error bars of the histogram are Poisson errors (\sqrt{N}).

At higher redshift thresholds, for instance $z_t = 3.0$, the same pipeline achieves an AUC of 0.877 and a TPR of 0.333. While the TPRs decline at higher z_t due to class imbalance and fewer high- z GRBs, our models still match or exceed the AUC values reported in earlier X-ray studies.

Another key distinction lies in the features used to train our models. We have included optical plateau emission properties, which were not considered in earlier studies besides our previous work (Dainotti et al., 2025), adding valuable information on GRB evolution at late times.

Thus, our optical redshift classifier has improved performance over prior classifiers built on prompt and X-ray properties, while also addressing limitations in earlier methodologies, such as a lack of test-validation splits, limited feature sets. This classifier serves as a more generalizable and scientifically grounded tool for real-time photometric classification of GRBs.

5.6. The user-friendly web-app

To make our work more accessible, we built a user-friendly web app using Streamlit, a tool to create interactive data science apps. The app can be run locally on any machine and is available on GitHub here: [Redshift-Classifer-Optical](#). Figure 15 shows parts of the app interface. The app allows users to customize the redshift classification process based on their needs. They can choose to apply the M-estimator for outlier removal using a threshold of their choice, apply MICE to handle

missing data, and set a custom value for z_t to adjust the GRB redshift classification.

If the M-estimator is not applied, the app uses the raw data in the SuperLearner pipeline after basic filtering (removing missing values and data points with $> 100\%$ relative error). If only MICE is selected, imputation is performed first, followed by SuperLearner. If only the M-estimator is selected, it runs before SuperLearner. If both MICE and the M-estimator are selected, the app applies the M-estimator, then MICE, and finally SuperLearner.

The SuperLearner pipeline performs LASSO-based feature and model selection with 100 nested 10-fold cross-validations, producing plots of selected features, model coefficients, and ROC-AUC scores for training and test sets.

6. Comparison with X-rays and Validation on the Generalisation Set

In this section, we apply the classifier developed for the X-ray redshift inference to the generalisation set from Narendra et al. (2025). This set—originally constructed for redshift regression—contains 263 LGRBs without spectroscopic redshifts but with plateau and prompt emission features, complemented by inferred redshifts from the regression model. Although this is not our standard validation set, this set becomes our validation set, because evaluating the classifier on it allows

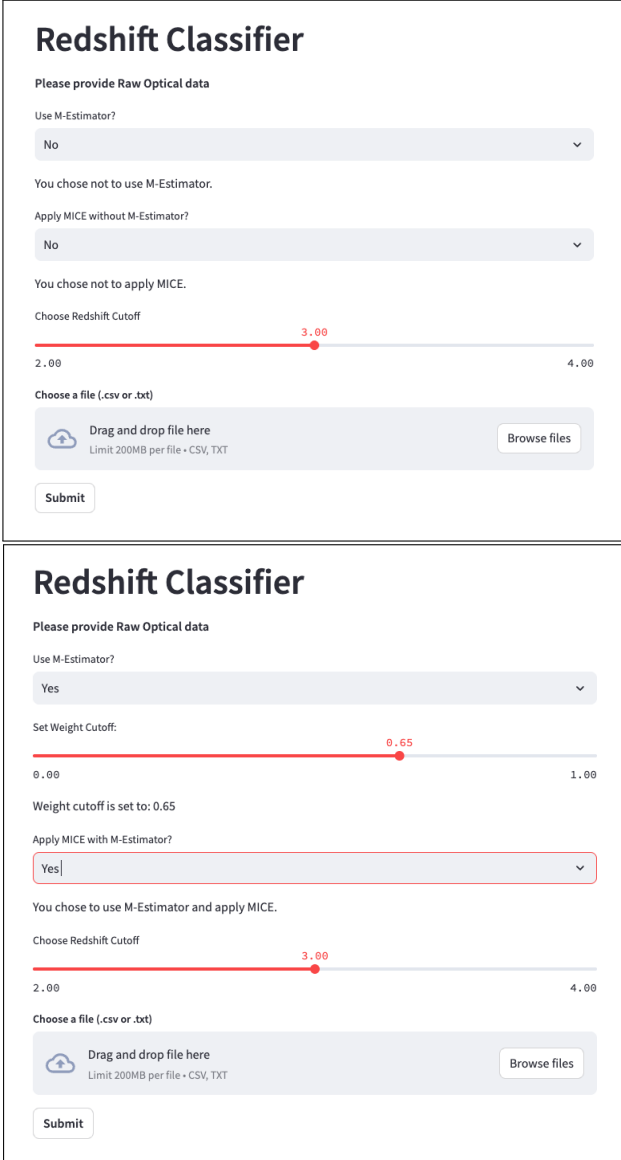


Figure 15: Up: shows the web-app interface when the user chooses not to apply both the M-estimator and MICE-imputation before running the SuperLearner. Down: depicts the web-app interface where the user chooses to apply both the M-estimator and MICE-imputation, followed by the SuperLearner. The user can select the desired value z_t within the web app before running the SuperLearner.

us to test whether the model can independently distinguish between low- and high-redshift GRBs, thereby offering an external consistency check on the regression-based redshift estimates.

To assess reliability, we validated the SuperLearner classifier trained with Mice imputation and the M-estimator threshold $z_t = 3.5$ on this independent sample. The classifier achieved an overall accuracy of 97.34%, with perfect specificity (100%) and conservative sensitivity (12.5%). The confusion matrix confirms this behaviour: the model correctly identified 255 GRBs as low- z with no false positives (i.e., no low- z event was mistakenly labelled as high- z), and among the true high- z candidates it identified only one true positive alongside seven false negatives.

This behaviour reflects the strongly precision-oriented calibration of the classifier. It is intentionally extremely cautious in assigning a high- z label and does so only when the feature evidence is exceptionally strong. As a result, the few predicted high- z events are highly reliable, but many genuine high- z bursts remain unflagged.

This trade-off between specificity and sensitivity is captured quantitatively by the moderate Cohen’s kappa (0.2169) and the balanced accuracy of 56.25%. Cohen’s kappa measures the agreement between predicted and true classes after accounting for chance alignment, meaning that it adjusts the raw accuracy by subtracting the level of agreement that would be expected if the classifier were assigning labels randomly according to the class frequencies. Unlike accuracy, it penalises classifiers that perform well simply by favouring the majority class. Thus, despite the high overall accuracy driven by the abundance of low- z bursts, the moderate kappa reflects the model’s limited recall on the minority high- z population.

The AUC curve (Fig. 16) further illustrates this precision–accuracy trade-off: achieving very high specificity necessarily limits sensitivity. The full SuperLearner ensemble attains an AUC of 0.9338, while the best-performing individual learner (the cforest model) achieves 0.9265. Overall, the classifier is suitable for strict, low-contamination high- z candidate selection, where the goal is to confidently flag not only the most secure high- z bursts, but also the low- z GRBs where intriguing cases of LGRBs associated with KNe may occur.

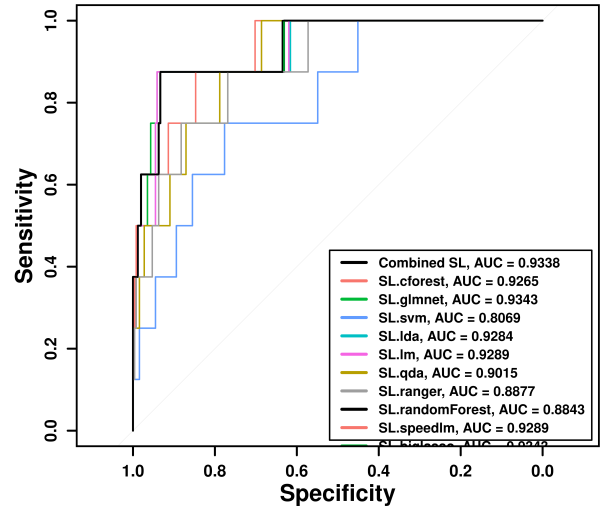


Figure 16: AUC curve for Generalisation Set

6.1. Comparison of Known Redshifts with X-ray Classifier and Estimator Results

A key objective of this work is to identify whether GRBs with known redshifts have consistent results with the X-ray classifier (Dainotti et al., 2025) and the regression-based estimator (Narendra et al., 2025). This classifier was trained with a cutoff at $z = 3.5$, producing a binary decision of low- z ver-

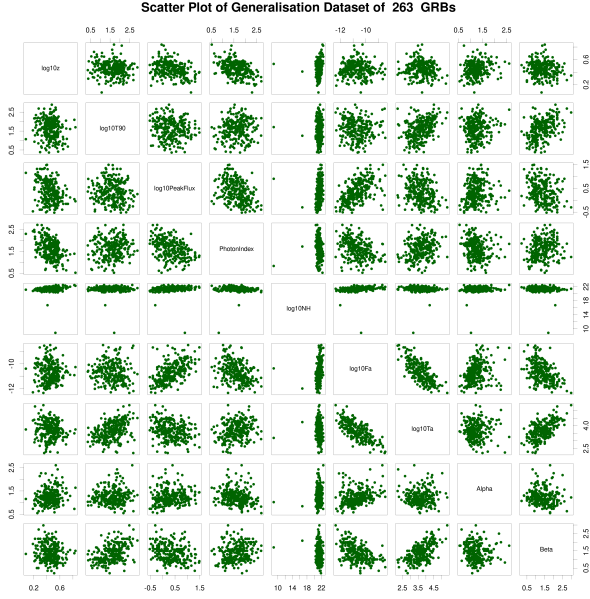


Figure 17: Feature scatter plot for generalisation set.

sus high- z . In contrast, the regression-based estimator provides continuous redshift predictions.

We searched for GRBs with known redshifts a posteriori from GRBweb (IceCube Collaboration, 2025) from the sample used for prediction and classification. This helps us to check the consistency and reliability of the estimator and classifier models. Figure 18 illustrates that GRBs with known redshifts and the predicted redshifts for the same GRBs do not closely follow the equality line. However, we note that the error bars of predicted redshifts are large, and thus we leave the conclusions more open. There are 38 cases for which the redshift is known which have been included in the generalization set for validation purposes. Out of the 38 cases, 28 GRBs have spectroscopically measured redshifts, and the remaining ten have tentative or photometric redshifts. We compared these 38 cases with the X-ray classifier results for a redshift threshold of 3.5. There is a $\sim 90\%$ agreement between the classifier results for a threshold of 3.5 and the redshifts from the GRBweb. This is compatible with the statement of sensitivity about classification (Dainotti et al., 2025). Only 4/38 cases have a mismatch (see Table 7) and the classifier predicts that they have $z < 3.5$, whereas their measured redshift are > 3.5 , identifying them as false negative. However, out of these 4 GRBs, 2 have redshifts measured photometrically and 2 are spectroscopic. So it may be possible that the redshift determination of these obtained by photometry is not accurate. Thus, conservatively, we need to exclude those cases as mismatches, hence the estimate of the true positive rate $\sim 92\%$.

We further searched for the redshifts of GRBs using photometric redshifts from the Dark Energy Spectroscopic Instrument Legacy Survey (DESI/LS) (Dey et al., 2019). Due to the magnitude limit of DESI/LS, the sample is restricted to GRBs with redshift $z < 1.5$. For GRBs with predicted red-

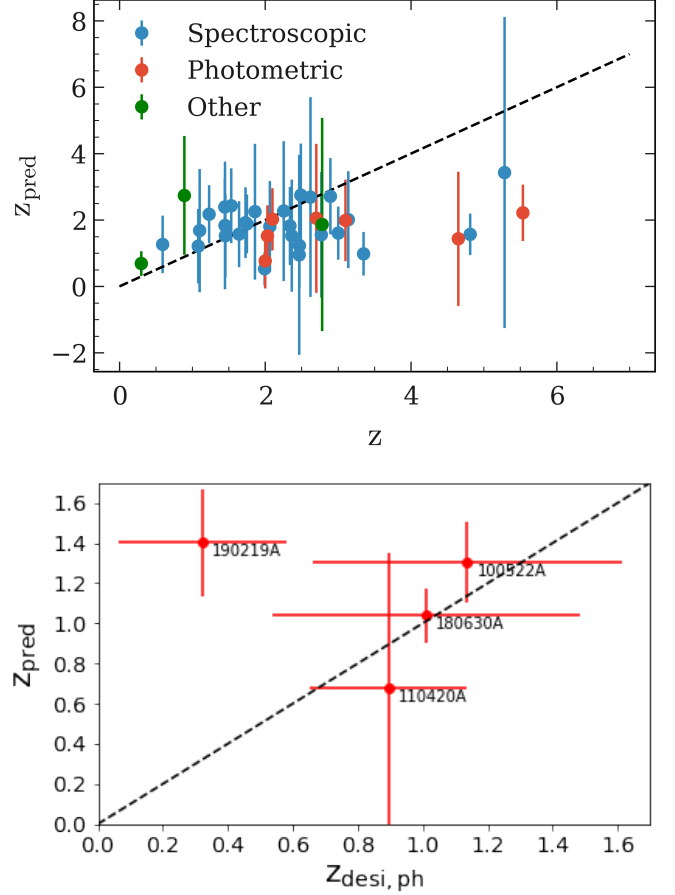


Figure 18: The figure indicates GRBs with known redshifts with values initially found using GRBweb. We also include their original reference in Table 7. The blue data points are GRBs with redshifts measured spectroscopically, while the red data points indicate GRBs with redshifts measured via photometry. The green data points are for GRB 130427B and GRB 150424A. The redshift for GRB 130427B is tentative, and the redshift of GRB 150424A is debated, as two of the references listed in Table 7 offer two possible values. The reference on the redshift of GRB 161001A indicates that the host galaxy is a candidate, not confirmed. The black dashed line represents the 1:1 case. Lower Panel: Comparison of DESI/LS photometric redshift and the predicted redshift.

shifts, we searched for galaxies within $5''$ of the GRB positions and recorded their photometric redshifts. The comparison between our predicted redshifts and the photometric redshifts is shown in the second panel of Figure 18. Our predictions are found to work well for objects with predicted redshifts below 1.2.

7. Summary and Conclusion

In this work, we introduce an ensemble ML framework designed to categorize GRBs based on their z , effectively distinguishing between those at high and low- z . Our analysis utilizes prompt, plateau, and afterglow emission features from 171 LGRBs observed by *Swift* UVOT and from 455 ground-based telescopes/detectors. The primary objective is to build and evaluate predictive models that can rapidly and reliably flag newly

GRB Redshift Comparison Table				
GRB	Redshift	Redshift Type	Reference	Agreement with classifier?
050814A	5.3 ± 0.3	photometric	(Jakobsson et al., 2006)	No
060108A	2.03	photometric	(Melandri et al., 2006)	Yes
060719A	1.532	spectroscopic	(Krühler et al., 2012)	Yes
060805A	2.363	spectroscopic	(Krühler et al., 2015)	Yes
061202A	2.2543	spectroscopic	(Krühler et al., 2015)	Yes
070103A	2.6208	spectroscopic	(Krühler et al., 2012)	Yes
070129A	2.3384	spectroscopic	(Krühler et al., 2012)	Yes
070224A	1.992	spectroscopic	(Krühler et al., 2015)	Yes
070328A	2.06	spectroscopic	(Krühler et al., 2015)	Yes
080605A	1.6403	spectroscopic	(Fynbo et al., 2009)	Yes
080707A	1.23	spectroscopic	(Fynbo et al., 2008)	Yes
081222A	2.77	spectroscopic	(Cucchiara et al., 2008)	Yes
090113A	1.7493	spectroscopic	(Krühler et al., 2012)	Yes
090407A	1.4478	spectroscopic	(Krühler et al., 2012)	Yes
100302A	4.813	spectroscopic	(Chornock et al., 2010)	No
100424A	2.4656	spectroscopic	(Malesani et al., 2013)	Yes
100522A	1.14 ± 0.47	photometric	This Work	Yes
110420A	0.89 ± 0.24	photometric	This Work	Yes
110801A	1.858	spectroscopic	(Cabrera Lavers et al., 2011)	Yes
111107A	2.893	spectroscopic	(Chornock et al., 2011)	Yes
111129A	1.080	spectroscopic	(Krühler et al., 2015)	Yes
120119A	1.728	spectroscopic	(Cucchiara and Prochaska, 2012)	Yes
120224A	1.1	spectroscopic	(Krühler et al., 2015)	Yes
121123A	2.7 ± 0.3	photometric	(Schmidl et al., 2012)	Yes
121209A	~ 2.1	photometric	(Krühler et al., 2015)	Yes
121217A	3.1 ± 0.1	photometric	(Elliott et al., 2014)	Yes
130427B	2.78 (tentative)	spectroscopic	(Flores et al., 2013)	Yes
140114A	3	spectroscopic	(Krühler et al., 2015)	Yes
140304A	5.283	spectroscopic	(de Ugarte Postigo et al., 2014b)	No
140331A	4.65	photometric	(Littlejohns et al., 2014)	No
140703A	3.14	spectroscopic	(Castro-Tirado et al., 2014)	Yes
141026A	3.35	spectroscopic	(de Ugarte Postigo et al., 2014a)	Yes
141221A	1.452	spectroscopic	(Perley et al., 2014)	Yes
150323A	0.593	spectroscopic	(Perley and Cenko, 2015)	Yes
150424A	$0.3 \text{ or } 1^{+0.3}_{-0.2}$	candidate host	(Castro-Tirado et al., 2015; Knust et al., 2017)	Yes
161001A	0.891	candidate host	(Selsing et al., 2019)	Yes
180115A	2.487	spectroscopic	(de Ugarte Postigo et al., 2018)	Yes
180314A	1.445	spectroscopic	(Sbarufatti et al., 2018)	Yes
180630A	1.01 ± 0.47	photometric	This Work	Yes
190219A	0.32 ± 0.26	photometric	This Work	No
190719C	2.469	spectroscopic	(Rossi et al., 2019)	Yes
210112A	~ 2	photometric	(Kann et al., 2021)	Yes

Table 7: All GRBs with known redshifts were used to test the consistency and reliability of the estimator and classifier model. Column 1: GRB name. Column 2: observed redshift. Column 3: method used to measure the redshift. Column 4: literature references.

observed GRBs as high- z events, thereby enabling timely follow-up and increasing their sample.

The classifier training pipeline comprises of several key steps, illustrated in Fig. 1) and summarized below:

1. Initial preprocessing involved discarding physically implausible entries and applying base-10 logarithmic trans-

formations to selected parameters.

2. Outlier detection and removal were conducted using the M-estimator method to ensure the reliability of the dataset.
3. Missing data were addressed through the MICE procedure.
4. Following the data preprocessing, LASSO was applied to extract the most informative features and reduce dimen-

sionality.

5. Model evaluation and selection were carried out via SuperLearner, implementing a nested CV to identify the best-performing models.
6. The final ensemble classifier was constructed using SuperLearner to maximize the AUC and sensitivity while minimizing Δ and overfitting.

A central novelty of our study is the incorporation of optical plateau-phase variables for the classification of high- z and low- z LGRBs. A similar technique has only been used in Dainotti et al. (2024a) for classification of high- z and low- z GRBs, and in Narendra et al. (2025) for z -estimation using regression, both using X-ray plateau phase features. Our results indicate that a threshold of $z_t = 2.0$ delivers the best classification accuracy for our particular dataset and model. Specifically, achieving an AUC of 84% for the raw dataset with M-Estimator with a high TPR of 0.741 and Δ varying between 1% and 4%.

Moreover, $z_t = 2.0$ consistently results in lower Δ across all our tested datasets compared to other thresholds.

We also introduce a public web application that enables the community to apply our machine-learning models for GRB redshift classification. The flexible design of this framework allows users to tailor the classifier to specific follow-up programs by adjusting sensitivity and specificity parameters.

This work demonstrates the significant potential of ensemble ML techniques in astrophysical research. By enabling more accurate identification of high- z and low- z LGRBs (the latter case is very important for the peculiar cases of KNe identified with the LGRBs), it lays the groundwork for expanding the known sample available for detailed photometric and spectroscopic investigation. A larger high- z LGRB dataset will, in turn, improve constraints on the GRB luminosity function and redshift evolution, offering deeper insights into the high- z universe.

A larger high- z LGRB dataset will allow us to settle on the problem of why the density rate at low- z GRB deviate from the general Star formation Rate evolution (Dainotti et al., 2024b; Petrosian and Dainotti, 2024; Bal et al., 2025; Khatiya et al., 2025).

Although reliable redshift estimators have been developed (Narendra et al., 2025; Dainotti et al., 2024a; Aldowma and Razzaque, 2024), our classifier provides an independent validation path for ML-based redshift estimation by verifying the redshift estimates predicted by these estimators.

The optical classifier complements the X-ray model of (Dainotti et al., 2024a), offering higher sensitivity to high- z events, while the X-ray version provides greater stability at larger redshift thresholds. Compared to earlier machine-learning efforts (Morgan et al., 2012; Ukwatta et al., 2016), our approach yields comparable or better AUC values with rigorous training-test validation and inclusion of optical plateau-phase features. Validation of the X-ray classifier on an independent generalization set confirms its reliability, and comparison with GRBs of known redshifts shows good consistency with both regression-based estimators and classifiers.

As both GRB datasets and ML algorithms continue to evolve, we expect significant gains in classification precision and recall in future research. Furthermore, the generalization of this framework makes it suitable for applications beyond GRBs, such as the classification of active galactic nuclei (AGN), possibly for BL Lacs due to the unavailability of absorption or emission lines in their optical spectra to perform spectroscopy. Our study advances the goal of utilizing GRBs as astrophysical probes of the early universe.

8. Acknowledgments

The authors thank the UK *Swift* Science Data Center at the University of Leicester for providing access to the *Swift* BAT+XRT data used in this study. MGD acknowledges the support of the DoS and by JSPS Grant-in-Aid for Scientific Research (KAKENHI) (A), Grant Number JP25H00675.

AP is grateful to the Polish National Science Centre grant 2023/50/A/ST9/00579. NF acknowledges financial support from UNAM-DGAPA-PAPIIT through grant IN112525. We acknowledge Aditya Narendra for his early help in setting up the analysis and guiding MS on writing the paper. We also thank the wider astrophysics community for maintaining and supporting publicly available datasets, which make independent research like this possible. In addition, we recognize the open-source software ecosystem that enabled our analysis and visualization workflows.

9. Data Availability

Data in this paper have been downloaded from the *Swift* BAT+XRT repository. This work made use of data provided by the UK *Swift* Science Data Centre located at the University of Leicester. Our Webapp is available for usage at Redshift-Classifer-Optical.

Appendix A. Redshift threshold of 2.0

Appendix A.1. Raw dataset without M-estimator

The SuperLearner shows a combined AUC value of 0.7622, with 'lm' as the individual best-performing algorithm, with an AUC value of 0.7785 and 'xgboost' as the individual least-performing algorithm, with an AUC value of 0.1909 (Figure 10 top left). When we removed the least-performing algorithms ('xgboost', 'ksvm', 'qda', 'earth'), the combined AUC increased marginally from 0.7622 to 0.7751 (Figure 10 top right).

Appendix A.2. Raw dataset with M-estimator

We apply the M-estimator to identify and remove the outliers (see Section 3.1). The SuperLearner yields an AUC value of 0.8261 on the training dataset. The best-performing individual algorithm is 'lda', with an AUC value of 0.8434, while 'ksvm' is the least-performing individual algorithm, with an AUC value of 0.7482 (Figure 10 second row left). By removing the least-performing algorithm ('ksvm'), the combined AUC value increased from 0.8261 to 0.8411 (Figure 10 second row right).

Appendix A.3. MICE-imputed dataset without M-estimator

We applied the MICE without the M-estimator. The combined performance of the SuperLearner on the training dataset yielded an AUC value of 0.6967. The highest-performing individual algorithms are 'lm' and 'speedlm', both with an AUC value of 0.714, while 'ranger' is the least-performing individual algorithm, with an AUC value of 0.6698 (Figure 10 bottom left). We also removed the less-performing algorithms ('randomforest', 'ranger'), which resulted in an increased combined AUC value from 0.6967 to 0.7061. (Figure 10 bottom right).

Appendix A.4. MICE-imputed dataset with M-estimator

We use MICE imputed data with the M-estimator. The combined performance of the SuperLearner on the training dataset resulted in an AUC value of 0.8021. The highest-performing individual algorithm is 'qda' with an AUC value of 0.8042, while 'kernelknn' is the least-performing individual algorithm, with an AUC value of 0.7078 (Figure 10 third row left). Removing the least-performing algorithm ('kernelKnn') resulted in a decrease in the combined AUC value from 0.8021 to 0.7817, and it is statistically insignificant (Figure 10 third row right).

Appendix B. Redshift threshold of 2.5

Appendix B.1. Raw dataset without M-estimator

The SuperLearner's combined performance on the training dataset yielded an AUC of 0.804, with 'speedlm' being the highest-performing individual algorithm (AUC = 0.8134), while 'caret.rpart' was the lowest-performing individual algorithm (AUC = 0.6221, Figure 11 top left). Upon removing the least performing algorithms ('caret.rpart', 'eartg', 'kernelKnn'), the combined AUC value increased slightly from 0.804 to 0.8071 (Figure 11 top right).

Appendix B.2. Raw dataset with M-estimator

The SuperLearner's combined performance on the training dataset achieved an AUC value of 0.8727. Among the individual algorithms, 'glmnet' performed the best with an AUC value of 0.8691, while 'svm' showed the lowest performance with an AUC value of 0.7082 (Figure 11 second row left). Removing the least performing algorithm ('svm') led to a slight increase in the combined AUC value from 0.8727 to 0.8773 (Figure 11 second row right).

Appendix B.3. MICE-imputed dataset without M-estimator

SuperLearner's combined performance on the training dataset achieved an AUC value of 0.7001. The best-performing individual algorithm is 'qda' with an AUC value of 0.7129, while 'xgboost' has the lowest individual AUC value of 0.6525 (Figure 11 bottom left). Removing the least-performing algorithm, 'xgboost', resulted in a slight decrease in the combined AUC from 0.7001 to 0.6524 (Figure 11 bottom right). This decrease in the combined AUC is not statistically significant.

Appendix B.4. MICE-imputed dataset with M-estimator

The combined performance of the SuperLearner on the training dataset resulted in an AUC value of 0.8343. The top-performing individual algorithm is 'qda', achieving an AUC value of 0.8316, while 'ksvm' performed the least with an AUC value of 0.73 (Figure 11 third row left). We also removed the least performing algorithms ('cforest' and 'ksvm'), which resulted in a decreased combined AUC value from 0.8343 to 0.8286 (Figure 11 third row right). This decrease in the combined AUC is not statistically significant.

Appendix C. Redshift threshold of 3.0

Appendix C.1. Raw dataset without M-estimator

The SuperLearner yielded a combined AUC value of 0.8, with 'xgboost' emerging as the individual best-performing algorithm with an AUC value of 0.9592 and 'ksvm' as the individual least-performing algorithm with AUC = 0.5893 (Figure 12 top left). When we removed the least-performing algorithms ('kernelKnn' and 'ksvm'), the combined AUC increased from 0.8 to 0.8095 (Figure 12 top right).

Appendix C.2. Raw dataset with M-estimator

The SuperLearner's combined performance on the training dataset yielded an AUC value of 0.8764. The best-performing individual algorithm is 'lm' with an AUC value of 0.8944, while 'lda' is the least-performing individual algorithm, with an AUC value of 0.8229 (Figure 12 second row left). By removing the least performing algorithms ('glm' and 'lda'), the combined AUC value decreased from 0.8764 to 0.875 (Figure 12 second row right). This decrease in the combined AUC is not statistically significant.

Appendix C.3. MICE-imputed dataset without M-estimator

The combined performance of the SuperLearner on the training dataset yielded an AUC value of 0.7354. The highest-performing individual algorithm is 'ranger' with an AUC value of 0.7434, while 'svm' is the least-performing individual algorithm, with an AUC value of 0.5826 (Figure 12 bottom left). We removed the less-performing algorithms ('bigLasso' and 'svm'), which resulted in an increased combined AUC value from 0.7354 to 0.7521 (Figure 12 bottom right).

Appendix C.4. MICE-imputed dataset with M-estimator

The combined performance of the SuperLearner on the training dataset resulted in an AUC value of 0.8197. The highest-performing individual algorithm is 'ksvm' with an AUC value of 0.832, while 'qda' is the least-performing individual algorithm, with an AUC value of 0.7066 (Figure 12 third row left). Removing the least-performing algorithms ('svm', 'qda' and 'kernelKnn') resulted in a decrease in the combined AUC value from 0.8197 to 0.8137 (Figure 12 third row right). This decrease in the combined AUC is not statistically significant (Jakobsson et al., 2006).

References

- Ahumada, T., Singer, L.P., Anand, S., Coughlin, M.W., Kasliwal, M.M., Ryan, G., Andreoni, I., Cenko, S.B., Fremling, C., Kumar, H., Pang, P.T.H., Burns, E., Cunningham, V., Dichiara, S., Dietrich, T., Svinkin, D.S., Almualla, M., Castro-Tirado, A.J., De, K., Dunwoody, R., Gatkine, P., Hammerstein, E., Iyyani, S., Mangan, J., Perley, D., Purkayastha, S., Bellm, E., Bhalerao, V., Bolin, B., Bulla, M., Cannella, C., Chandra, P., Duev, D.A., Frederiks, D., Gal-Yam, A., Graham, M., Ho, A.Y.Q., Hurley, K., Karambelkar, V., Kool, E.C., Kulkarni, S.R., Mahabal, A., Masci, F., McBreen, S., Pandey, S.B., Reusch, S., Ridnaia, A., Rosnet, P., Rusholme, B., Carracedo, A.S., Smith, R., Soumagnac, M., Stein, R., Troja, E., Tsvetkova, A., Walters, R., Valeev, A.F., 2021. Discovery and confirmation of the shortest gamma-ray burst from a collapsar. *Nature Astronomy* 5, 917–927. doi:10.1038/s41550-021-01428-7, arXiv:2105.05067.
- Aldowma, T., Razzaque, S., 2024. Deep Neural Networks for estimation of gamma-ray burst redshifts. *Monthly Notices of the Royal Astronomical Society* 529, 2676–2685. doi:10.1093/mnras/stae535, arXiv:2401.11005.
- Bal, D.S., Narendra, A., Dainotti, M.G., Khatiya, N.S., Lenart, A.L., Hartmann, D.H., 2025. Probing evolution of long grb properties through their cosmic formation history aided by machine learning predicted redshifts. URL: <https://arxiv.org/abs/2510.07306>, arXiv:2510.07306.
- Barthelmy, S.D., Chincarini, G., Burrows, D.N., Gehrels, N., Covino, S., Moretti, A., Romano, P., O’Brien, P.T., Sarazin, C.L., Kouveliotou, C., Goad, M., Vaughan, S., Tagliaferri, G., Zhang, B., Antonelli, L.A., Campana, S., Cummings, J.R., D’Avanzo, P., Davies, M.B., Giommi, P., Grupe, D., Kaneko, Y., Kennea, J.A., King, A., Kobayashi, S., Melandri, A., Meszaros, P., Nousek, J.A., Patel, S., Sakamoto, T., Wijers, R.A.M.J., 2005. An origin for short γ -ray bursts unassociated with current star formation. *Nature* 438, 994–996. doi:10.1038/nature04392, arXiv:astro-ph/0511579.
- Berger, E., 2008. The host galaxies of short-duration gamma-ray bursts: Luminosities, metallicities, and star formation rates. *The Astrophysical Journal* 690, 231–237. URL: <http://dx.doi.org/10.1088/0004-637X/690/1/231>, doi:10.1088/0004-637x/690/1/231.
- Beskin, G., Karpov, S., Bondar, S., Greco, G., Guarnieri, A., Bartolini, C., Piccioni, A., 2010. Fast Optical Variability of a Naked-eye Burst—Manifestation of the Periodic Activity of an Internal Engine. *ApJL* 719, L10–L14. doi:10.1088/2041-8205/719/1/L10, arXiv:0905.4431.
- Bhardwaj, S., Dainotti, M.G., Venkatesh, S., Narendra, A., Kalsi, A., Rinaldi, E., Pollo, A., 2023. GRB optical and X-ray plateau properties classifier using unsupervised machine learning. *Monthly Notices of the Royal Astronomical Society* 525, 5204–5223. URL: <https://doi.org/10.1093/mnras/stad2593>, doi:10.1093/mnras/stad2593.
- Birnbaum, A., 1962. On the foundations of statistical inference. *JASA* 57, 269–306.
- Breiman, L., 2001. Random forests. *Machine Learning* 45, 5–32. URL: <http://dx.doi.org/10.1023/A%3A1010933404324>, doi:10.1023/A:1010933404324.
- Breiman, L., Friedman, J., Olshen, R., Stone, C., 1984. *Classification and Regression Trees*. Chapman and Hall/CRC. doi:<https://doi.org/10.1201/9781315139470>.
- Bromm, V., Loeb, A., 2006. High-redshift gamma-ray bursts from population iii progenitors. *The Astrophysical Journal* 642, 382–388. URL: <http://dx.doi.org/10.1086/500799>, doi:10.1086/500799.
- Brown, S.D., Tauler, R., Walczak, B. (Eds.), 2009. *Comprehensive Chemometrics: Chemical and Biochemical Data Analysis*. Elsevier. doi:10.1016/B978-0-444-64163-0.X0001-7.
- Burrows, D.N., Hill, J.E., Nousek, J.A., Kennea, J.A., Wells, A., Osborne, J.P., Abbey, A.F., Beardmore, A., Mukerjee, K., Short, A.D.T., Chincarini, G., Campana, S., Citterio, O., Moretti, A., Pagani, C., Tagliaferri, G., Giommi, P., Capalbi, M., Tamburelli, F., Angelini, L., Cusumano, G., Bräuninger, H.W., Burkert, W., Hartner, G.D., 2005. The Swift X-Ray Telescope. *SSRv* 120, 165–195. doi:10.1007/s11214-005-5097-2, arXiv:astro-ph/0508071.
- van Buuren, S., Groothuis-Oudshoorn, K., 2011. mice: Multivariate imputation by chained equations in r. *JSS* 45, 1–67. URL: <https://www.jstatsoft.org/index.php/jss/article/view/v045i03>, doi:10.18637/jss.v045.i03.
- Cabrera Lavers, A., de Ugarte Postigo, A., Castro-Tirado, A.J., Gorosabel, J., Thoene, C.C., Dominguez, R., 2011. GRB 110801A: afterglow redshift from 10.4m GTC. *GRB Coordinates Network* 12234, 1.
- Campana, S., Tagliaferri, G., Malesani, D., Stella, L., D’Avanzo, P., Chincarini, G., Covino, S., 2007. Near real-time selection of high redshift GRBs with Swift. *Astronomy & Astrophysics* 464, L25–L27. doi:10.1051/0004-6361:20066592, arXiv:astro-ph/0610626.
- Castro-Tirado, A.J., Cunniffe, R., Sanchez-Ramirez, R., Gorosabel, J., Jelinek, M., Oates, S.R., Jeong, S., Tello, J.R., Pandey, S., 2014. GRB140703A: 10.4m GTC redshift. *GRB Coordinates Network* 16505, 1.
- Castro-Tirado, A.J., Sanchez-Ramirez, R., Lombardi, G., Rivero, M.A., 2015. GRB 150424A: 10.4m GTC spectroscopy. *GRB Coordinates Network* 17758, 1.
- Chawla, N.V., Bowyer, K.W., Hall, L.O., Kegelmeyer, W.P., 2002. Smote: synthetic minority over-sampling technique. *Journal of artificial intelligence research* 16, 321–357.

- Chen, T., Guestrin, C., 2016. Xgboost: A scalable tree boosting system, in: Proceedings of the 22nd acm sigkdd international conference on knowledge discovery and data mining, pp. 785–794.
- Chornock, R., Berger, E., Fox, D., 2011. GRB 111107A: gemini-south redshift. GRB Coordinates Network 12537, 1.
- Chornock, R., Cucchiara, A., Fox, D., Berger, E., 2010. GRB 100302A: gemini-north redshift. GRB Coordinates Network 10466, 1.
- Cortes, C., Vapnik, V., 1995. Support-vector networks. *Machine learning* 20, 273–297. doi:10.1007/BF00994018.
- Costa, E., Frontera, F., Heise, J., Feroci, M., in't Zand, J., Fiore, F., Cinti, M.N., Dal Fiume, D., Nicastro, L., Orlandini, M., Palazzi, E., Rapisarda, M., Zavattini, G., Jager, R., Parmar, A., Owens, A., Molendi, S., Cusumano, G., Maccarone, M.C., Giarrusso, S., Coletta, A., Antonelli, L.A., Giommi, P., Muller, J.M., Piro, L., Butler, R.C., 1997. Discovery of an X-ray afterglow associated with the γ -ray burst of 28 February 1997. *Nature* 387, 783–785. doi:10.1038/42885, arXiv:astro-ph/9706065.
- Cucchiara, A., Fox, D.B., Cenko, S.B., Berger, E., 2008. GRB 081222: gemini-south absorption redshift. GRB Coordinates Network 8713, 1.
- Cucchiara, A., Levan, A.J., Fox, D.B., Tanvir, N.R., Ukwatta, T.N., Berger, E., Krühler, T., Küpcü Yoldaş, A., Wu, X.F., Toma, K., Greiner, J., Olivares, F.E., Rowlinson, A., Amati, L., Sakamoto, T., Roth, K., Stephens, A., Fritz, A., Fynbo, J.P.U., Hjorth, J., Malesani, D., Jakobsson, P., Wiersema, K., O'Brien, P.T., Soderberg, A.M., Foley, R.J., Fruchter, A.S., Rhoads, J., Rutledge, R.E., Schmidt, B.P., Dopita, M.A., Podsiadlowski, P., Willingale, R., Wolf, C., Kulkarni, S.R., D'Avanzo, P., 2011. A Photometric Redshift of $z \sim 9.4$ for GRB 090429B. *ApJ* 736, 7. doi:10.1088/0004-637X/736/1/7, arXiv:1105.4915.
- Cucchiara, A., Prochaska, J.X., 2012. GRB 120119A: gemini-south redshift. GRB Coordinates Network 12865, 1.
- Cusumano, G., Mangano, V., Chincarini, G., Panaitescu, A., Burrows, D.N., La Parola, V., Sakamoto, T., Campana, S., Mineo, T., Tagliaferri, G., Angelini, L., Barthelmy, S.D., Beardmore, A.P., Boyd, P.T., Cominsky, L.R., Gronwall, C., Fenimore, E.E., Gehrels, N., Giommi, P., Goad, M., Hurley, K., Kennea, J.A., Mason, K.O., Marshall, F., Mészáros, P., Nousek, J.A., Osborne, J.P., Palmer, D.M., Roming, P.W.A., Wells, A., White, N.E., Zhang, B., 2006. Gamma-ray bursts: Huge explosion in the early Universe. *Nature* 440, 164. doi:10.1038/440164a, arXiv:astro-ph/0509737.
- Cusumano, G., Mangano, V., Chincarini, G., Panaitescu, A., Burrows, D.N., La Parola, V., Sakamoto, T., Campana, S., Mineo, T., Tagliaferri, G., Angelini, L., Barthelmy, S.D., Beardmore, A.P., Boyd, P.T., Cominsky, L.R., Gronwall, C., Fenimore, E.E., Gehrels, N., Giommi, P., Goad, M., Hurley, K., Immler, S., Kennea, J.A., Mason, K.O., Marshall, F., Mészáros, P., Nousek, J.A., Osborne, J.P., Palmer, D.M., Roming, P.W.A., Wells, A., White, N.E., Zhang, B., 2007. Swift observations of GRB 050904: the most distant cosmic explosion ever observed. *Astronomy & Astrophysics* 462, 73–80. doi:10.1051/0004-6361:20065173, arXiv:astro-ph/0610570.
- Dainotti, M.G., Bhardwaj, S., Cook, C., Ange, J., Lamichhane, N., Bogdan, M., McGee, M., Nadolsky, P., Sarkar, M., Pollo, A., Nagataki, S., 2024a. Grb redshift classifier to follow-up high-redshift grbs using supervised machine learning. URL: <https://arxiv.org/abs/2408.08763>, arXiv:2408.08763.
- Dainotti, M.G., Bhardwaj, S., Cook, C., Ange, J., Lamichhane, N., Bogdan, M., McGee, M., Nadolsky, P., Sarkar, M., Pollo, A., Nagataki, S., 2025. Grb redshift classifier to follow up high-redshift grbs using supervised machine learning. *The Astrophysical Journal Supplement Series* 277, 31. URL: <https://doi.org/10.3847/1538-4365/adafa9>, doi:10.3847/1538-4365/adafa9.
- Dainotti, M.G., Bhardwaj, S., Cook, C., Ange, J., Lamichhane, N., Bogdan, M., McGee, M., Nadolsky, P., Sarkar, M., Pollo, A., Nagataki, S., 2025. GRB Redshift Classifier to Follow up High-redshift GRBs Using Supervised Machine Learning. *Astrophys. J. Suppl.* 277, 31. doi:10.3847/1538-4365/adafa9, arXiv:2408.08763.
- Dainotti, M.G., Bogdan, M., Narendra, A., Gibson, S.J., Missojedor, B., Lioudakis, I., Pollo, A., Nelson, T., Wozniak, K., Nguyen, Z., Larrison, J., 2021. Predicting the redshift of γ -ray-loud AGNs using supervised machine learning. *ApJ* 920, 118. URL: <https://doi.org/10.3847/1538-4357/ac1748>, doi:10.3847/1538-4357/ac1748.
- Dainotti, M.G., Cardone, V.F., Capozziello, S., 2008. A time-luminosity correlation for γ -ray bursts in the X-rays. *MNRAS* 391, L79–L83. doi:10.1111/j.1745-3933.2008.00560.x, arXiv:0809.1389.
- Dainotti, M.G., Fabrizio Cardone, V., Capozziello, S., Ostrowski, M., Willingale, R., 2011. Study of Possible Systematics in the L^*_X - T^*_a Correlation of Gamma-ray Bursts. *ApJ* 730, 135. doi:10.1088/0004-637X/730/2/135, arXiv:1101.1676.
- Dainotti, M.G., Livermore, S., Kann, D.A., Li, L., Oates, S., Yi, S., Zhang, B., Gendre, B., Cenko, B., Fraija, N., 2020a. The Optical Luminosity-Time Correlation for More than 100 Gamma-Ray Burst Afterglows. *ApJL* 905, L26. doi:10.3847/2041-8213/abcda9, arXiv:2011.14493.
- Dainotti, M.G., Livermore, S., Kann, D.A., Li, L., Oates, S., Yi, S., Zhang, B., Gendre, B., Cenko, B., Fraija, N., 2020b. The Optical Luminosity-Time Correlation for More than 100 Gamma-Ray Burst Afterglows. *The Astrophysical Journal Letters* 905, L26. doi:10.3847/2041-8213/abcda9, arXiv:2011.14493.

- Dainotti, M.G., Narendra, A., Pollo, A., Petrosian, V., Bogdan, M., Iwasaki, K., Prochaska, J.X., Rinaldi, E., Zhou, D., 2024b. Gamma-ray bursts as distance indicators by a statistical learning approach. *Astrophys. J. Letter*. 967, L30. doi:10.3847/2041-8213/ad4970, arXiv:2402.04551.
- Dainotti, M.G., Omodei, N., Srinivasaragavan, G.P., Vianello, G., Willingale, R., O'Brien, P., Nagataki, S., Petrosian, V., Nuygen, Z., Hernandez, X., Axelsson, M., Bissaldi, E., Longo, F., 2021. On the Existence of the Plateau Emission in High-energy Gamma-Ray Burst Light Curves Observed by Fermi-LAT. *ApJS* 255, 13. doi:10.3847/1538-4365/abfe17, arXiv:2105.07357.
- Dainotti, M.G., Taira, E., Wang, E., Lehman, E., Narendra, A., Pollo, A., Madejski, G.M., Petrosian, V., Bogdan, M., Dey, A., Bhardwaj, S., 2024a. Inferring the redshift of more than 150 grbs with a machine-learning ensemble model. *The Astrophysical Journal Supplement Series* 271, 22. URL: <https://dx.doi.org/10.3847/1538-4365/ad1aaf>, doi:10.3847/1538-4365/ad1aaf.
- Dainotti, M.G., Young, S., Li, L., Levine, D., Kalinowski, K.K., Kann, D.A., Tran, B., Zambrano-Tapia, L., Zambrano-Tapia, A., Cenko, S.B., Fuentes, M., Sánchez-Vázquez, E.G., Oates, S.R., Fraija, N., Becerra, R.L., Watson, A.M., Butler, N.R., González, J.J., Kutyrev, A.S., Lee, W.H., Prochaska, J.X., Ramirez-Ruiz, E., Richer, M.G., Zola, S., 2022a. The Optical Two- and Three-dimensional Fundamental Plane Correlations for Nearly 180 Gamma-Ray Burst Afterglows with Swift/UVOT, RATIR, and the Subaru Telescope. *The Astrophysical Journal Supplement Series* 261, 25. doi:10.3847/1538-4365/ac7c64, arXiv:2203.12908.
- Dainotti, M.G., Young, S., Li, L., Levine, D., Kalinowski, K.K., Kann, D.A., Tran, B., Zambrano-Tapia, L., Zambrano-Tapia, A., Cenko, S.B., Fuentes, M., Sánchez-Vázquez, E.G., Oates, S.R., Fraija, N., Becerra, R.L., Watson, A.M., Butler, N.R., González, J.J., Kutyrev, A.S., Lee, W.H., Prochaska, J.X., Ramirez-Ruiz, E., Richer, M.G., Zola, S., 2022b. The Optical Two- and Three-dimensional Fundamental Plane Correlations for Nearly 180 Gamma-Ray Burst Afterglows with Swift/UVOT, RATIR, and the Subaru Telescope. *Astrophys. J. Suppl.* 261, 25. doi:10.3847/1538-4365/ac7c64, arXiv:2203.12908.
- de Menezes, D., Prata, D., Secchi, A., Pinto, J., 2021. A review on robust m-estimators for regression analysis. *Computers & Chemical Engineering* 147, 107254. URL: <https://www.sciencedirect.com/science/article/pii/S0098135421000326>, doi:<https://doi.org/10.1016/j.compchemeng.2021.107254>.
- de Ugarte Postigo, A., Cano, Z., Izzo, L., Thoene, C.C., Kann, D.A., Castro-Rodriguez, N., Valladares, D.P., 2018. GRB 180115A: Redshift from OSIRIS/GTC. *GRB Coordinates Network* 22346, 1.
- de Ugarte Postigo, A., Thoene, C.C., Tanvir, N.R., Gorosabel, J., Fynbo, J., Lombardi, G., Reverte-Paya, D., Perez, D., 2014a. GRB 141026A: GTC spectroscopy. *GRB Coordinates Network* 16968, 1.
- de Ugarte Postigo, A., Xu, D., Gorosabel, J., Malesani, D., Milvang-Jensen, B., Andersen, M.I., Jakobsson, P., Fynbo, J.P.U., Somero, A., 2014b. GRB 140304A: redshift from the NOT. *GRB Coordinates Network* 15924, 1.
- Dey, A., Schlegel, D.J., Lang, D., Blum, R., Burleigh, K., Fan, X., Findlay, J.R., Finkbeiner, D., Herrera, D., Juneau, S., Landriau, M., Levi, M., McGreer, I., Meisner, A., Myers, A.D., Moustakas, J., Nugent, P., Patej, A., Schlafly, E.F., Walker, A.R., Valdes, F., Weaver, B.A., Yèche, C., Zou, H., Zhou, X., Abareshi, B., Abbott, T.M.C., Abolfathi, B., Aguilera, C., Alam, S., Allen, L., Alvarez, A., Annis, J., Ansarinejad, B., Aubert, M., Beechert, J., Bell, E.F., Ben-Zvi, S.Y., Beutler, F., Bielby, R.M., Bolton, A.S., Briceño, C., Buckley-Geer, E.J., Butler, K., Calamida, A., Carlberg, R.G., Carter, P., Casas, R., Castander, F.J., Choi, Y., Comparat, J., Cukanovaite, E., Delubac, T., DeVries, K., Dey, S., Dhungana, G., Dickinson, M., Ding, Z., Donaldson, J.B., Duan, Y., Duckworth, C.J., Eftekharzadeh, S., Eisenstein, D.J., Etourneau, T., Fagrelus, P.A., Farihi, J., Fitzpatrick, M., Font-Ribera, A., Fulmer, L., Gänsicke, B.T., Gaztanaga, E., George, K., Gerdes, D.W., Gontcho, S.G.A., Gorgoni, C., Green, G., Guy, J., Harmer, D., Hernandez, M., Honscheid, K., Huang, L.W., James, D.J., Jannuzi, B.T., Jiang, L., Joyce, R., Karcher, A., Karkar, S., Kehoe, R., Kneib, J.P., Kueter-Young, A., Lan, T.W., Lauer, T.R., Le Guillou, L., Le Van Suu, A., Lee, J.H., Lesser, M., Perreault Levasseur, L., Li, T.S., Mann, J.L., Marshall, R., Martínez-Vázquez, C.E., Martini, P., du Mas des Bourboux, H., McManus, S., Meier, T.G., Ménard, B., Metcalfe, N., Muñoz-Gutiérrez, A., Najita, J., Napier, K., Narayan, G., Newman, J.A., Nie, J., Nord, B., Norman, D.J., Olsen, K.A.G., Paat, A., Palanque-Delabrouille, N., Peng, X., Poppett, C.L., Poremba, M.R., Prakash, A., Rabinowitz, D., Raichoor, A., Rezaie, M., Robertson, A.N., Roe, N.A., Ross, A.J., Ross, N.P., Rudnick, G., Safonova, S., Saha, A., Sánchez, F.J., Savary, E., Schweiker, H., Scott, A., Seo, H.J., Shan, H., Silva, D.R., Slepian, Z., Soto, C., Sprayberry, D., Staten, R., Stillman, C.M., Stupak, R.J., Summers, D.L., Sien Tie, S., Tirado, H., Vargas-Magaña, M., Vivas, A.K., Wechsler, R.H., Williams, D., Yang, J., Yang, Q., Yapici, T., Zaritsky, D., Zenteno, A., Zhang, K., Zhang, T., Zhou, R., Zhou, Z., 2019. Overview of the DESI Legacy Imaging Surveys. *Astron. J.* 157, 168. doi:10.3847/1538-3881/ab089d, arXiv:1804.08657.
- Elliott, J., et al., 2014. Prompt emission of GRB 121217A from gamma-rays to the near-infrared. *Astron. Astrophys.* 562, A100. doi:10.1051/0004-6361/201322600, arXiv:1312.4547.
- Enea, M., 2009. Fitting linear models and generalized linear models with large data sets in r, in: *Fitting Linear Models and Generalized Linear Models with large data sets in R*, pp. 411–414.

- Evans, P.A., Beardmore, A.P., Page, K.L., Osborne, J.P., O'Brien, P.T., Willingale, R., Starling, R.L.C., Burrows, D.N., Godet, O., Vetere, L., Racusin, J., Goad, M.R., Wiersema, K., Angelini, L., Capalbi, M., Chincarini, G., Gehrels, N., Kennea, J.A., Margutti, R., Morris, D.C., Mountford, C.J., Pagani, C., Perri, M., Romano, P., Tanvir, N., 2009. Methods and results of an automatic analysis of a complete sample of Swift-XRT observations of GRBs. *MNRAS* 397, 1177–1201. doi:10.1111/j.1365-2966.2009.14913.x, arXiv:0812.3662.
- Fausey, H.M., Vejlgaard, S., van der Horst, A.J., Heintz, K.E., Izzo, L., Malesani, D.B., Wiersema, K., Fynbo, J.P.U., Tanvir, N.R., Vergani, S.D., Saccardi, A., Rossi, A., Campana, S., Covino, S., D'Elia, V., Pasquale, M.D., Hartmann, D., Jakobsson, P., Kouveliotou, C., Levan, A., Martin-Carrillo, A., Melandri, A., Palmerio, J., Pugliese, G., Salvaterra, R., 2024. Neutral fraction of hydrogen in the intergalactic medium surrounding high-redshift gamma-ray burst 210905a. URL: <https://arxiv.org/abs/2403.13126>, arXiv:2403.13126.
- Flores, H., Covino, S., de Ugarte Postigo, A., Fynbo, J., Kruehler, T., Xu, D., Tanvir, N., 2013. GRB 130427B: tentative VLT/X-shooter redshift. *GRB Coordinates Network* 14493, 1.
- Fox, J., 2015. *Applied Regression Analysis and Generalized Linear Models*. SAGE Publications.
- Frail, D.A., Cameron, P.B., Kasliwal, M., Nakar, E., Price, P.A., Berger, E., Gal-Yam, A., Kulkarni, S.R., Fox, D.B., Soderberg, A.M., Schmidt, B.P., Ofek, E., Cenko, S.B., 2006. An Energetic Afterglow from a Distant Stellar Explosion. *ApJL* 646, L99–L102. doi:10.1086/506934, arXiv:astro-ph/0604580.
- Friedman, J., Hastie, T., Tibshirani, R., 2001. *The elements of statistical learning*. Springer Series in statistics, Springer, New York, NY, USA.
- Friedman, J., Hastie, T., Tibshirani, R., 2010. Regularization paths for generalized linear models via coordinate descent. *Journal of statistical software* 33, 1.
- Friedman, J., Hastie, T., Tibshirani, R., et al., 2000. Additive logistic regression: a statistical view of boosting (with discussion and a rejoinder by the authors). *Annals of statistics* 28, 337–407.
- Friedman, J.H., Roosen, C.B., 1995. An introduction to multivariate adaptive regression splines. *Statistical Methods in Medical Research* 4, 197–217. URL: <https://doi.org/10.1177/096228029500400303>, doi:10.1177/096228029500400303, arXiv:<https://doi.org/10.1177/096228029500400303>. PMID: 8548103.
- Fynbo, J.P.U., Jakobsson, P., Prochaska, J.X., Malesani, D., Ledoux, C., de Ugarte Postigo, A., Nardini, M., Vreeswijk, P.M., Wiersema, K., Hjorth, J., Sollerman, J., Chen, H.W., Thöne, C.C., Björnsson, G., Bloom, J.S., Castro-Tirado, A.J., Christensen, L., De Cia, A., Fruchter, A.S., Gorosabel, J., Graham, J.F., Jaunsen, A.O., Jensen, B.L., Kann, D.A., Kouveliotou, C., Levan, A.J., Maund, J., Masetti, N., Milvang-Jensen, B., Palazzi, E., Perley, D.A., Pian, E., Rol, E., Schady, P., Starling, R.L.C., Tanvir, N.R., Watson, D.J., Xu, D., Augusteijn, T., Grundahl, F., Telting, J., Quirion, P.O., 2009. Low-resolution Spectroscopy of Gamma-ray Burst Optical Afterglows: Biases in the Swift Sample and Characterization of the Absorbers. *Astrophys. J. Suppl.* 185, 526–573. doi:10.1088/0067-0049/185/2/526, arXiv:0907.3449.
- Fynbo, J.P.U., Malesani, D., Milvang-Jensen, B., 2008. GRB 080707: VLT redshift. *GRB Coordinates Network* 7949, 1.
- Gehrels, N., Chincarini, G., Giommi, P., Mason, K.O., Nousek, J.A., Wells, A.A., White, N.E., Barthelmy, S.D., Burrows, D.N., Cominsky, L.R., Hurley, K.C., Marshall, F.E., Mészáros, P., Roming, P.W.A., Angelini, L., Barbier, L.M., Belloni, T., Campana, S., Caraveo, P.A., Chester, M.M., Citterio, O., Cline, T.L., Cropper, M.S., Cummings, J.R., Dean, A.J., Feigelson, E.D., Fenimore, E.E., Frail, D.A., Fruchter, A.S., Garmire, G.P., Gendreau, K., Ghisellini, G., Greiner, J., Hill, J.E., Hunsberger, S.D., Krimm, H.A., Kulkarni, S.R., Kumar, P., Lebrun, F., Lloyd-Ronning, N.M., Markwardt, C.B., Mattson, B.J., Mushotzky, R.F., Norris, J.P., Osborne, J., Paczynski, B., Palmer, D.M., Park, H.S., Parsons, A.M., Paul, J., Rees, M.J., Reynolds, C.S., Rhoads, J.E., Sasseen, T.P., Schaefer, B.E., Short, A.T., Smale, A.P., Smith, I.A., Stella, L., Tagliaferri, G., Takahashi, T., Tashiro, M., Townsley, L.K., Tueller, J., Turner, M.J.L., Vietri, M., Voges, W., Ward, M.J., Willingale, R., Zerbi, F.M., Zhang, W.W., 2004. The Swift Gamma-Ray Burst Mission. *ApJ* 611, 1005–1020. doi:10.1086/422091, arXiv:astro-ph/0405233.
- Geurts, P., Ernst, D., Wehenkel, L., 2006. Extremely randomized trees. *Machine Learning* 63, 42–63. doi:10.1007/s10994-006-6226-1.
- Gibson, S.J., Narendra, A., Dainotti, M.G., Bogdan, M., Pollo, A., Poliszczuk, A., Rinaldi, E., Liodakis, I., 2022. Using multivariate imputation by chained equations to predict redshifts of active galactic nuclei. *Frontiers in Astronomy and Space Sciences* 9. URL: <https://www.frontiersin.org/article/10.3389/fspas.2022.836215>, doi:10.3389/fspas.2022.836215.
- Gorbovskoy, E.S., Lipunova, G.V., Lipunov, V.M., Kornilov, V.G., Belinski, A.A., Shatskiy, N.I., Tyurina, N.V., Kuvshinov, D.A., Balanutsa, P.V., Chazov, V.V., Kuznetsov, A., Zimnukhov, D.S., Kornilov, M.V., Sankovich, A.V., Krylov, A., Ivanov, K.I., Chvalaev, O., Poleschuk, V.A., Konstantinov, E.N., Gress, O.A., Yazev, S.A., Budnev, N.M., Krushinski, V.V., Zalozhnych, I.S., Popov, A.A., Tlatov, A.G., Parhomenko, A.V., Dormidontov, D.V., Senik, V., Yurkov, V.V., Sergienko, Y.P., Varda, D., Kudelina, I.P.,

- Castro-Tirado, A.J., Gorosabel, J., Sánchez-Ramírez, R., Jelinek, M., Tello, J.C., 2012. Prompt, early and afterglow optical observations of five γ -ray bursts: GRB 100901A, GRB 100902A, GRB 100905A, GRB 100906A and GRB 101020A. *MNRAS* 421, 1874–1890. doi:10.1111/j.1365-2966.2012.20195.x, arXiv:1111.3625.
- Greiner, J., Krühler, T., Klose, S., et al., 2011. The nature of dark gamma-ray bursts. *Astronomy & Astrophysics* 526, A30. doi:10.1051/0004-6361/201015458.
- Grupe, D., Nousek, J.A., vanden Berk, D.E., Roming, P.W.A., Burrows, D.N., Godet, O., Osborne, J., Gehrels, N., 2007. Redshift Filtering by Swift Apparent X-Ray Column Density. *The Astronomical Journal* 133, 2216–2221. doi:10.1086/513014, arXiv:astro-ph/0612104.
- Hastie, T., Tibshirani, R., 1987. Generalized additive models: some applications. *Journal of the American Statistical Association* 82, 371–386. doi:10.2307/2289439.
- Hastie, T., Tibshirani, R., Friedman, J., 2009. *The elements of statistical learning: data mining, inference, and prediction*. Springer Science & Business Media.
- Hastie, T.J., Tibshirani, R.J., 1990. Generalized additive models. volume 43. CRC press. doi:10.1201/9780203753781.
- Ho, T.K., 1995. Random decision forests, in: *Proceedings of 3rd international conference on document analysis and recognition*, IEEE. pp. 278–282.
- Huber, P.J., 1964a. Robust Estimation of a Location Parameter. *The Annals of Mathematical Statistics* 35, 73 – 101. URL: <https://doi.org/10.1214/aoms/1177703732>, doi:10.1214/aoms/1177703732.
- Huber, P.J., 1964b. Robust Estimation of a Location Parameter. *The Annals of Mathematical Statistics* 35, 73 – 101. URL: <https://doi.org/10.1214/aoms/1177703732>, doi:10.1214/aoms/1177703732.
- Huber, P.J., 1996. *Robust statistical procedures*. SIAM.
- Huber, P.J., Ronchetti, E.M., 2009. *Robust Statistics*. 2nd ed., Wiley. doi:10.1002/9780470434697.
- IceCube Collaboration, 2025. GRBweb: A Catalog of Gamma-Ray Bursts. https://user-web.icecube.wisc.edu/~grbweb_public/.
- Jakobsson, P., Levan, A., Fynbo, J.P.U., Priddey, R., Hjorth, J., Tanvir, N., Watson, D., Jensen, B.L., Sollerman, J., Natarajan, P., Gorosabel, J., Castro Cerón, J.M., Pedersen, K., Purshino, T., Árnadóttir, A.S., Castro-Tirado, A.J., Davis, C.J., Deeg, H.J., Fiuza, D.A., Mikolaitis, S., Sousa, S.G., 2006. A mean redshift of 2.8 for Swift gamma-ray bursts. *Astronomy & Astrophysics* 447, 897–903. doi:10.1051/0004-6361:20054287, arXiv:astro-ph/0509888.
- Jakobsson, P., et al., 2006. A mean redshift of 2.8 for swift gamma-ray bursts. *Astron. Astrophys.* 447, 897–903. doi:10.1051/0004-6361:20054287, arXiv:astro-ph/0509888.
- Kann, D.A., de Ugarte Postigo, A., Thoene, C.C., Blazek, M., Agui Fernandez, J.F., Sota, A., 2021. GRB 210112A: OSN Reddened Afterglow Detection. *GRB Coordinates Network* 29296, 1.
- Kann, D.A., Klose, S., Zeh, A., 2006. Signatures of Extragalactic Dust in Pre-Swift GRB Afterglows. *ApJ* 641, 993–1009. doi:10.1086/500652, arXiv:astro-ph/0512575.
- Karatzoglou, A., Smola, A., Hornik, K., Zeileis, A., 2004. kernlab - an s4 package for kernel methods in r. *Journal of Statistical Software* 11, 1–20. URL: <https://www.jstatsoft.org/index.php/jss/article/view/v011i09>, doi:10.18637/jss.v011.i09.
- Karson, M., 1968. *Handbook of methods of applied statistics. volume i: Techniques of computation descriptive methods, and statistical inference. volume ii: Planning of surveys and experiments.* i. m. chakravarti, r. g. laha, and j. roy, new york, john wiley; 1967, \$9.00. *Journal of the American Statistical Association* 63, 1047–1049. URL: <https://doi.org/10.1080/01621459.1968.11009335>, doi:10.1080/01621459.1968.11009335, arXiv:<https://doi.org/10.1080/01621459.1968.11009335>.
- Khatiya, N.S., Dainotti, M.G., Narendra, A., Bal, D.S., Lenart, A.L., Hartmann, D.H., 2025. Probing evolution of long gamma-ray burst properties through their cosmic formation history. *The Astrophysical Journal* 990, 69. URL: <http://dx.doi.org/10.3847/1538-4357/adf219>, doi:10.3847/1538-4357/adf219.
- Knust, F., et al., 2017. Long optical plateau in the afterglow of the short GRB 150424A with extended emission - Evidence for energy injection by a magnetar? *Astron. Astrophys.* 607, A84. doi:10.1051/0004-6361/201730578, arXiv:1707.01329.
- Koen, C., 2009. Multiple regression of GRB luminosity on light-curve properties. *Monthly Notices of the Royal Astronomical Society* 396, 1499–1506. doi:10.1111/j.1365-2966.2009.14795.x.
- Koen, C., 2010. Predicting gamma-ray burster redshifts from their prompt emission properties. *Monthly Notices of the Royal Astronomical Society* 401, 1369–1374. doi:10.1111/j.1365-2966.2009.15737.x.
- Kouveliotou, C., Meegan, C.A., Fishman, G.J., Bhat, N.P., Briggs, M.S., Koshut, T.M., Paciesas, W.S., Pendleton, G.N., 1993. Identification of Two Classes of Gamma-Ray Bursts. *The Astrophysical Journal Letters* 413, L101. doi:10.1086/186969.

- Krühler, T., Malesani, D., Milvang-Jensen, B., Fynbo, J.P.U., Hjorth, J., Jakobsson, P., Levan, A.J., Sparre, M., Tanvir, N.R., Watson, D.J., 2012. The Optically Unbiased GRB Host (TOUGH) Survey. V. VLT/X-shooter Emission-line Redshifts for Swift GRBs at $z \sim 2$. *Astrophys. J.* 758, 46. doi:10.1088/0004-637X/758/1/46, arXiv:1205.4036.
- Krühler, T., et al., 2015. GRB hosts through cosmic time - VLT/X-Shooter emission-line spectroscopy of 96 γ -ray-burst-selected galaxies at $0.1 < z < 3.6$. *Astron. Astrophys.* 581, A125. doi:10.1051/0004-6361/201425561, arXiv:1505.06743.
- Kumar, P., Zhang, B., 2015. The physics of gamma-ray bursts & relativistic jets. *Physics Reports* 561, 1–109. doi:10.1016/j.physrep.2014.09.008, arXiv:1410.0679.
- Van der Laan, M.J., Polley, E.C., Hubbard, A.E., 2007. Super learner. *Statistical applications in genetics and molecular biology* 6.
- Lamb, D.Q., 2002. Gamma-Ray Bursts as a Probe of Cosmology, in: Gilfanov, M., Sunyeav, R., Churazov, E. (Eds.), *Lighthouses of the Universe: The Most Luminous Celestial Objects and Their Use for Cosmology*, p. 157. doi:10.1007/10856495_20.
- Lamb, D.Q., Reichart, D.E., 2000. Gamma-ray bursts as a probe of the very high redshift universe, in: Kippen, R.M., Mallozzi, R.S., Fishman, G.J. (Eds.), *Gamma-ray Bursts, 5th Huntsville Symposium*, pp. 658–662. doi:10.1063/1.1361618.
- Levesque, E.M., Bloom, J.S., Butler, N.R., Perley, D.A., Cenko, S.B., Prochaska, J.X., Kewley, L.J., Bunker, A., Chen, H.W., Chornock, R., Filippenko, A.V., Glazebrook, K., Lopez, S., Masiero, J., Modjaz, M., Morgan, A., Poznanski, D., 2010. GRB090426: the environment of a rest-frame 0.35-s gamma-ray burst at a redshift of 2.609. *MNRAS* 401, 963–972. doi:10.1111/j.1365-2966.2009.15733.x, arXiv:0907.1661.
- Levine, D., Dainotti, M., Zvonarek, K.J., Fraija, N., Warren, D.C., Chandra, P., Lloyd-Ronning, N., 2022. Examining Two-dimensional Luminosity-Time Correlations for Gamma-Ray Burst Radio Afterglows with VLA and ALMA. *ApJ* 925, 15. doi:10.3847/1538-4357/ac4221, arXiv:2111.10428.
- Li, L., Wu, X.F., Lei, W.H., Dai, Z.G., Liang, E.W., Ryde, F., 2018. Constraining the Type of Central Engine of GRBs with Swift Data. *ApJ Supplement* 236, 26. doi:10.3847/1538-4365/aabaf3, arXiv:1712.09390.
- Li, L.X., 2008. Star formation history up to $z = 7.4$: implications for gamma-ray bursts and cosmic metallicity evolution. *Monthly Notices of the Royal Astronomical Society* 388, 1487–1500. URL: <http://dx.doi.org/10.1111/j.1365-2966.2008.13488.x>, doi:10.1111/j.1365-2966.2008.13488.x.
- Liang, E.W., Zhang, B.B., Zhang, B., 2007. A Comprehensive Analysis of Swift XRT Data. II. Diverse Physical Origins of the Shallow Decay Segment. *ApJ* 670, 565–583. doi:10.1086/521870, arXiv:0705.1373.
- Little, R.J., Rubin, D.B., 2019. *Statistical analysis with missing data*. volume 793. John Wiley & Sons. doi:10.1002/9781119013563.
- Littlejohns, O., Butler, N., Watson, A.M., Kutyrev, A., Lee, W.H., Richer, M.G., Klein, C., Fox, O., Prochaska, J.X., Bloom, J., Cucchiara, A., Troja, E., Ramirez-Ruiz, E., de Diego, J.A., Georgiev, L., Gonzalez, J., Roman-Zuniga, C., Gehrels, N., Moseley, H., 2014. GRB 140331A: RATIR Optical and NIR Observations. *GRB Coordinates Network* 16050, 1.
- Malesani, D., Xu, D., Fynbo, J.P.U., Kruehler, T., Perley, D.A., Vergani, S.D., Goldoni, P., 2013. GRB 100424A: Keck host detection and VLT/X-shooter redshift. *GRB Coordinates Network* 14291, 1.
- Mazets, E.P., Golenetskii, S.V., Ilinskii, V.N., Panov, V.N., Aptekar, R.L., Gurian, I.A., Proskura, M.P., Sokolov, I.A., Sokolova, Z.I., Kharitonova, T.V., 1981. Catalog of cosmic gamma-ray bursts from the KONUS experiment data. *Ap&SS* 80, 3–83. doi:10.1007/BF00649140.
- McLachlan, G.J., 2004. *Discriminant Analysis and Statistical Pattern Recognition*. Wiley-Interscience.
- Melandri, A., Grazian, A., Guidorzi, C., Monfardini, A., Mundell, C.G., Gomboc, A., 2006. GRB060108: photometric redshift determination. *GRB Coordinates Network* 4539, 1.
- Morgan, A.N., Long, J., Richards, J.W., Broderick, T., Butler, N.R., Bloom, J.S., 2012. Rapid, Machine-learned Resource Allocation: Application to High-redshift Gamma-Ray Burst Follow-up. *ApJ* 746, 170. doi:10.1088/0004-637X/746/2/170, arXiv:1112.3654.
- Narendra, A., Dainotti, M.G., Sarkar, M., Lenart, A.L., Bogdan, M., Pollo, A., Zhang, B., Rabeda, A., Petrosian, V., Iwasaki, K., 2025. Gamma-ray burst redshift estimation using machine learning and the associated web app. *Astronomy & Astrophysics* 698, A92. URL: <http://dx.doi.org/10.1051/0004-6361/202452651>, doi:10.1051/0004-6361/202452651.
- Narendra, A., Gibson, S.J., Dainotti, M.G., Bogdan, M., Pollo, A., Liodakis, I., Poliszczuk, A., Rinaldi, E., 2022. Predicting the redshift of gamma-ray loud AGNs using supervised machine learning ii. *ApJ Supplement Series* 259, 55. URL: <https://doi.org/10.3847/1538-4365/ac545a>, doi:10.3847/1538-4365/ac545a.
- Nelder, J.A., Wedderburn, R.W., 1972a. Generalized linear models. *Journal of the Royal Statistical Society: Series A (General)* 135, 370–384.

- Nelder, J.A., Wedderburn, R.W.M., 1972b. Generalized linear models. *Journal of the Royal Statistical Society. Series A (General)* 135, 370–384. URL: <http://www.jstor.org/stable/2344614>.
- Norris, J.P., Bonnell, J.T., 2006. Short Gamma-Ray Bursts with Extended Emission. *ApJ* 643, 266–275. doi:10.1086/502796, arXiv:astro-ph/0601190.
- Nousek, J.A., Kouveliotou, C., Grupe, D., Page, K.L., Granot, J., Ramirez-Ruiz, E., Patel, S.K., Burrows, D.N., Mangano, V., Barthelmy, S., Beardmore, A.P., Campana, S., Capalbi, M., Chincarini, G., Cusumano, G., Falcone, A.D., Gehrels, N., Giommi, P., Goad, M.R., Godet, O., Hurkett, C.P., Kennea, J.A., Moretti, A., O’Brien, P.T., Osborne, J.P., Romano, P., Tagliaferri, G., Wells, A.A., 2006. Evidence for a Canonical Gamma-Ray Burst Afterglow Light Curve in the Swift XRT Data. *ApJ* 642, 389–400. doi:10.1086/500724, arXiv:astro-ph/0508332.
- Oates, S.R., Page, M.J., De Pasquale, M., Schady, P., Breeveld, A.A., Holland, S.T., Kuin, N.P.M., Marshall, F.E., 2012. A correlation between the intrinsic brightness and average decay rate of Swift/UVOT gamma-ray burst optical/ultraviolet light curves. *MNRAS* 426, L86–L90. doi:10.1111/j.1745-3933.2012.01331.x, arXiv:1208.1856.
- O’Brien, P.T., Willingale, R., Osborne, J., Goad, M.R., Page, K.L., Vaughan, S., Rol, E., Beardmore, A., Godet, O., Hurkett, C.P., Wells, A., Zhang, B., Kobayashi, S., Burrows, D.N., Nousek, J.A., Kennea, J.A., Falcone, A., Grupe, D., Gehrels, N., Barthelmy, S., Cannizzo, J., Cummings, J., Hill, J.E., Krimm, H., Chincarini, G., Tagliaferri, G., Campana, S., Moretti, A., Giommi, P., Perri, M., Mangano, V., LaParola, V., 2006. The Early X-Ray Emission from GRBs. *ApJ* 647, 1213–1237. doi:10.1086/505457, arXiv:astro-ph/0601125.
- Oganesyan, G., Nava, L., Ghirlanda, G., Melandri, A., Celotti, A., 2019. Prompt optical emission as a signature of synchrotron radiation in gamma-ray bursts. *Astronomy & Astrophysics* 628, A59. URL: <http://dx.doi.org/10.1051/0004-6361/201935766>, doi:10.1051/0004-6361/201935766.
- Panaitescu, A., Vestrand, W.T., 2008. Taxonomy of gamma-ray burst optical light curves: identification of a salient class of early afterglows. *MNRAS* 387, 497–504. doi:10.1111/j.1365-2966.2008.13231.x, arXiv:0803.1872.
- Panaitescu, A., Vestrand, W.T., 2011. Optical afterglows of gamma-ray bursts: peaks, plateaus and possibilities. *MNRAS* 414, 3537–3546. doi:10.1111/j.1365-2966.2011.18653.x, arXiv:1009.3947.
- Perley, D.A., Cao, Y., Cenko, S.B., 2014. GRB 141221A: Keck spectroscopy. *GRB Coordinates Network* 17228, 1.
- Perley, D.A., Cenko, S.B., 2015. GRB 150323A: Keck redshift. *GRB Coordinates Network* 17616, 1.
- Perley, D.A., Cenko, S.B., Bloom, J.S., et al., 2009. The hosts of dark gamma-ray bursts. *Astronomical Journal* 138, 1690–1708. doi:10.1088/0004-6256/138/6/1690.
- Perley, D.A., Krühler, T., Schulze, S., et al., 2013. The swift gamma-ray burst host galaxy legacy survey. *Astrophysical Journal* 778, 128. doi:10.1088/0004-637X/778/2/128.
- Petrosian, V., Dainotti, M.G., 2024. Progenitors of Low-redshift Gamma-Ray Bursts. *The Astrophysical Journal Letters* 963, L12. doi:10.3847/2041-8213/ad2763, arXiv:2305.15081.
- Piro, L., Amati, L., Antonelli, L.A., Butler, R.C., Costa, E., Cusumano, G., Feroci, M., Frontera, F., Heise, J., in ’t Zand, J.J.M., Molendi, S., Muller, J., Nicastro, L., Orlandini, M., Owens, A., Parmar, A.N., Soffitta, P., Tavani, M., 1998. Evidence for a late-time outburst of the X-ray afterglow of GB970508 from BeppoSAX. *A&A* 331, L41–L44. arXiv:astro-ph/9710355.
- Polley, E.C., Rose, S., van der Laan, M.J., 2011. Super learning, in: *Targeted Learning: Causal Inference for Observational and Experimental Data*. Springer New York, New York, NY, pp. 43–66.
- Prochaska, J.X., Chen, H.W., Bloom, J.S., 2006. Dissecting the circumburst and interstellar medium of gamma-ray bursts through afterglow spectroscopy. *Astrophysical Journal* 648, 95–105. doi:10.1086/505138.
- Prochaska, J.X., Chen, H.W., Bloom, J.S., et al., 2007. The host galaxies of gamma-ray bursts. *Astrophysical Journal Supplement Series* 168, 231–251. doi:10.1086/511026.
- Prochaska, J.X., Chen, H.W., Dessauges-Zavadsky, M., Bloom, J.S., 2008. The galactic environments of gamma-ray bursts. *Astrophysical Journal* 672, 59–85. doi:10.1086/523701.
- Prochaska, J.X., Sheffer, Y., Perley, D.A., et al., 2009. The host galaxies of swift gamma-ray bursts: Constraints on the progenitors and environments. *Astrophysical Journal* 691, L27–L31. doi:10.1088/0004-637X/691/1/L27.
- R Core Team, 2022. *R: A Language and Environment for Statistical Computing*. R Foundation for Statistical Computing. Vienna, Austria. URL: <https://www.R-project.org/>.
- Rastinejad, J.C., Gompertz, B.P., Levan, A.J., O’Connor, B., Fong, W., Perley, D.A., Troja, E., Tanvir, N.R., Schroeder, G., et al., 2022. A kilonova following a long-duration gamma-ray burst at 350 mpc. *Nature* 612, 223–226. doi:10.1038/s41586-022-05465-6.
- Roming, P.W., Schady, P., Fox, D.B., Zhang, B., Liang, E., Mason, K.O., Rol, E., Burrows, D.N., Blustin, A.J., Boyd, P.T., et al., 2006. Very early optical afterglows of gamma-ray bursts: evidence for relative paucity of detection. *ApJ* 652, 1416.

- Roming, P.W.A., Kennedy, T.E., Mason, K.O., Nousek, J.A., Ahr, L., Bingham, R.E., Broos, P.S., Carter, M.J., Hancock, B.K., Huckle, H.E., Hunsberger, S.D., Kawakami, H., Killough, R., Koch, T.S., McLelland, M.K., Smith, K., Smith, P.J., Soto, J.C., Boyd, P.T., Breeveld, A.A., Holland, S.T., Ivanushkina, M., Pryzby, M.S., Still, M.D., Stock, J., 2005. The Swift Ultra-Violet/Optical Telescope. *SSRv* 120, 95–142. doi:10.1007/s11214-005-5095-4, arXiv:astro-ph/0507413.
- Rossi, A., Heintz, K.E., Fynbo, J.P.U., Malesani, D.B., de Ugarte Postigo, A., Vergani, S.D., Kann, D.A., Thoene, C.C., Izzo, L., Campana, S., Pugliese, G., Kaper, L., Kouveliotou, C., Tanvir, N.R., Stargate Collaboration, 2019. GRB 190719C: VLT/X-shooter spectroscopic redshift of the host galaxy. *GRB Coordinates Network* 25252, 1.
- Rowlinson, A., Gompertz, B.P., Dainotti, M., O’Brien, P.T., Wijers, R.A.M.J., van der Horst, A.J., 2014. Constraining properties of GRB magnetar central engines using the observed plateau luminosity and duration correlation. *MNRAS* 443, 1779–1787. doi:10.1093/mnras/stu1277, arXiv:1407.1053.
- Rubin, D.B., 1976. Inference and missing data. *Biometrika* 63, 581–592. URL: <http://www.jstor.org/stable/2335739>, doi:10.2307/2335739.
- Sakamoto, T., Hill, J.E., Yamazaki, R., Angelini, L., Krimm, H.A., Sato, G., Swindell, S., Takami, K., Osborne, J.P., 2007. Evidence of Exponential Decay Emission in the Swift Gamma-Ray Bursts. *ApJ* 669, 1115–1129. doi:10.1086/521640, arXiv:0707.2170.
- Salvaterra, R., Campana, S., Chincarini, G., Tagliaferri, G., Covino, S., 2007. On the detection of very high redshift gamma-ray bursts with Swift. *Monthly Notices of the Royal Astronomical Society* 380, L45–L48. doi:10.1111/j.1745-3933.2007.00345.x, arXiv:0706.0657.
- Sbarufatti, B., Bolmer, J., de Ugarte Postigo, A., Fynbo, J.P.U., Selsing, J., Heintz, K.E., Malesani, D., Tanvir, N.R., Levan, A.J., Smette, A., Wiersema, K., Covino, S., 2018. GRB 180314A: VLT/X-shooter redshift. *GRB Coordinates Network* 22484, 1.
- Schafer, J.L., Graham, J.W., 2002. Missing data: our view of the state of the art. *Psychological methods* 7, 147. doi:10.1037/1082-989X.7.2.147.
- Schmidl, S., Nicuesa Guelbenzu, A., Klose, S., Greiner, J., 2012. GRB 121123A: GROND observations. *GRB Coordinates Network* 13992, 1.
- Selsing, J., et al., 2019. The X-shooter GRB afterglow legacy sample (XS-GRB). *Astron. Astrophys.* 623, A92. doi:10.1051/0004-6361/201832835, arXiv:1802.07727.
- Shen, R.F., Zhang, B., 2009. Prompt optical emission and synchrotron self-absorption constraints on emission site of grbs. *Monthly Notices of the Royal Astronomical Society* 398, 1936–1950. URL: <http://dx.doi.org/10.1111/j.1365-2966.2009.15212.x>, doi:10.1111/j.1365-2966.2009.15212.x.
- Simon, N., Friedman, J.H., Hastie, T., Tibshirani, R., 2011. Regularization paths for cox’s proportional hazards model via coordinate descent. *Journal of Statistical Software* 39, 1–13. URL: <https://www.jstatsoft.org/index.php/jss/article/view/v039i05>, doi:10.18637/jss.v039.i05.
- Srinivasaragavan, G.P., Dainotti, M.G., Fraija, N., Hernandez, X., Nagataki, S., Lenart, A., Bowden, L., Wagner, R., 2020. On the Investigation of the Closure Relations for Gamma-Ray Bursts Observed by Swift in the Post-plateau Phase and the GRB Fundamental Plane. *ApJ* 903, 18. doi:10.3847/1538-4357/abb702, arXiv:2009.06740.
- Tibshirani, R., 1996. Regression shrinkage and selection via the lasso. *Journal of the Royal Statistical Society Series B* 58, 267.
- Toma, K., Yoon, S.C., Bromm, V., 2016. Gamma-ray bursts and population iii stars. *Space Science Reviews* 202, 159–180. URL: <http://dx.doi.org/10.1007/s11214-016-0250-7>, doi:10.1007/s11214-016-0250-7.
- Torsten Hothorn, K.H., Zeileis, A., 2006. Unbiased recursive partitioning: A conditional inference framework. *Journal of Computational and Graphical Statistics* 15, 651–674. URL: <https://doi.org/10.1198/106186006X133933>, doi:10.1198/106186006X133933, arXiv:https://doi.org/10.1198/106186006X133933.
- Ukwatta, T.N., Sakamoto, T., Dhuga, K.S., Parke, W.C., Barthelmy, S.D., Gehrels, N., Stamatikos, M., Tueller, J., 2009. Investigating the Possibility of Screening High-z GRBs based on BAT Prompt Emission Properties, in: Meegan, C., Kouveliotou, C., Gehrels, N. (Eds.), *Gamma-ray Burst: Sixth Huntsville Symposium*, AIP. pp. 437–439. doi:10.1063/1.3155945, arXiv:0901.2928.
- Ukwatta, T.N., Sakamoto, T., Stamatikos, M., Gehrels, N., Dhuga, K.S., 2008. Screening High-z GRBs with BAT Prompt Emission Properties, in: Galassi, M., Palmer, D., Fenimore, E. (Eds.), *Gamma-ray Bursts 2007*, AIP. pp. 166–169. doi:10.1063/1.2943435, arXiv:0802.3815.
- Ukwatta, T.N., Woźniak, P.R., Gehrels, N., 2016. Machine-z: rapid machine-learned redshift indicator for Swift gamma-ray bursts. *MNRAS* 458, 3821–3829. doi:10.1093/mnras/stw559, arXiv:1512.07671.
- van Paradijs, J., Groot, P.J., Galama, T., Kouveliotou, C., Strom, R.G., Telting, J., Rutten, R.G.M., Fishman, G.J., Meegan, C.A., Pettini, M., Tanvir, N., Bloom, J., Pedersen, H., Nørdgaard-Nielsen, H.U., Linden-Vørnle, M., Melnick, J., Van der Steene, G., Bremer, M., Naber, R., Heise, J., in’t

- Zand, J., Costa, E., Feroci, M., Piro, L., Frontera, F., Zavatini, G., Nicastro, L., Palazzi, E., Bennett, K., Hanlon, L., Parmar, A., 1997. Transient optical emission from the error box of the γ -ray burst of 28 February 1997. *Nature* 386, 686–689. doi:10.1038/386686a0.
- vanden Berk, D.E., Grupe, D., Racusin, J., Roming, P., Koch, S., 2008. Selection of High-Redshift GRB Candidates from Rapidly Available Swift Data, in: Galassi, M., Palmer, D., Fenimore, E. (Eds.), *Gamma-ray Bursts 2007*, AIP. pp. 80–83. doi:10.1063/1.2943555.
- Vapnik, V.N., 1995. *The Nature of Statistical Learning Theory*. Springer-Verlag New York, Inc., New York, NY.
- Venables, W.N., Ripley, B.D., 2002. *Modern Applied Statistics with S*. Fourth ed., Springer, New York. URL: <https://www.stats.ox.ac.uk/pub/MASS4/>. ISBN 0-387-95457-0.
- Vestrand, W.T., Wozniak, P.R., Wren, J.A., Fenimore, E.E., Sakamoto, T., White, R.R., Casperson, D., Davis, H., Evans, S., Galassi, M., McGowan, K.E., Schier, J.A., Asa, J.W., Barthelmy, S.D., Cummings, J.R., Gehrels, N., Hullinger, D., Krimm, H.A., Markwardt, C.B., McLean, K., Palmer, D., Parsons, A., Tueller, J., 2005. A link between prompt optical and prompt γ -ray emission in γ -ray bursts. *Nature* 435, 178–180. doi:10.1038/nature03515, arXiv:astro-ph/0503521.
- Vestrand, W.T., Wren, J.A., Panaitescu, A., Wozniak, P.R., Davis, H., Palmer, D.M., Vianello, G., Omodei, N., Xiong, S., Briggs, M.S., Elphick, M., Paciesas, W., Rosing, W., 2014. The Bright Optical Flash and Afterglow from the Gamma-Ray Burst GRB 130427A. *Science* 343, 38–41. doi:10.1126/science.1242316, arXiv:1311.5489.
- Wager, S., Athey, S., 2017. Estimation and inference of heterogeneous treatment effects using random forests. arXiv:1510.04342.
- Wang, F.Y., 2013. The high-redshift star formation rate derived from gamma-ray bursts: possible origin and cosmic reionization. *Astronomy & Astrophysics* 556, A90. URL: <http://dx.doi.org/10.1051/0004-6361/201321623>, doi:10.1051/0004-6361/201321623.
- Yu, K., Ji, L., Zhang, X., 2002. Kernel nearest neighbor algorithm. *Neural Processing Letters* 15, 147–156. doi:10.1023/A:1015244902967.
- Zaninoni, E., Bernardini, M.G., Margutti, R., Oates, S., Chincarini, G., 2013. Gamma-ray burst optical light-curve zoo: comparison with X-ray observations. *A&A* 557, A12. doi:10.1051/0004-6361/201321221, arXiv:1303.6924.
- Zeh, A., Klose, S., Kann, D.A., 2006. Gamma-Ray Burst Afterglow Light Curves in the Pre-Swift Era: A Statistical Study. *ApJ* 637, 889–900. doi:10.1086/498442, arXiv:astro-ph/0509299.
- Zeng, Y., Breheny, P., 2017. The biglasso package: A memory- and computation-efficient solver for lasso model fitting with big data in r. arXiv preprint arXiv:1701.05936 .
- Zhang, B., 2014. Gamma-ray burst prompt emission. *International Journal of Modern Physics D* 23, 1430002. URL: <https://doi.org/10.1142/S021827181430002X>, doi:10.1142/S021827181430002X, arXiv:<https://doi.org/10.1142/S021827181430002X>.
- Zhang, B., 2018. *The Physics of Gamma-Ray Bursts*. Cambridge University Press. doi:10.1017/9781139226530.
- Zhang, B., Fan, Y.Z., Dyks, J., Kobayashi, S., Mészáros, P., Burrows, D.N., Nousek, J.A., Gehrels, N., 2006. Physical Processes Shaping Gamma-Ray Burst X-Ray Afterglow Light Curves: Theoretical Implications from the Swift X-Ray Telescope Observations. *ApJ* 642, 354–370. doi:10.1086/500723, arXiv:astro-ph/0508321.
- Zhang, B., Mészáros, P., 2004. Gamma-Ray Bursts: progress, problems & prospects. *Int J Mod Phys A* 19, 2385–2472. doi:10.1142/S0217751X0401746X, arXiv:astro-ph/0311321.
- Zhang, B., Zhang, B.B., Virgili, F.J., Liang, E.W., Kann, D.A., Wu, X.F., Proga, D., Lv, H.J., Toma, K., Mészáros, P., Burrows, D.N., Roming, P.W.A., Gehrels, N., 2009. Discerning the Physical Origins of Cosmological Gamma-ray Bursts Based on Multiple Observational Criteria: The Cases of $z = 6.7$ GRB 080913, $z = 8.2$ GRB 090423, and Some Short/Hard GRBs. *ApJ* 703, 1696–1724. doi:10.1088/0004-637X/703/2/1696, arXiv:0902.2419.
- Zhang, B.B., Zhang, B., Murase, K., Connaughton, V., Briggs, M.S., 2014. How long does a burst burst? *ApJ* 787, 66. URL: <https://dx.doi.org/10.1088/0004-637X/787/1/66>, doi:10.1088/0004-637X/787/1/66.
- Zou, H., Hastie, T., 2005. Regularization and Variable Selection Via the Elastic Net. *Journal of the Royal Statistical Society Series B: Statistical Methodology* 67, 301–320. URL: <https://doi.org/10.1111/j.1467-9868.2005.00503.x>, doi:10.1111/j.1467-9868.2005.00503.x.